Title	Factors that differentiate the H-bond strengths of water near the Schiff bases in bacteriorhodopsin and Anabaena sensory rhodopsin.
Author(s)	Saito, Keisuke; Kandori, Hideki; Ishikita, Hiroshi
Citation	The Journal of biological chemistry (2012), 287(41): 34009-34018
Issue Date	2012-10-05
URL	http://hdl.handle.net/2433/169708
Right	This research was originally published in "Journal of Biological Chemistry". Saito K., Kandori H., Ishikita H. Factors that differentiate the H-bond strengths of water near the schiff bases in bacteriorhodopsin and Anabaena sensory rhodopsin. 2012;287:34009-34018. © the American Society for Biochemistry and Molecular Biology.
Type	Journal Article
Textversion	author

Factors that differentiate the H-bond strengths of water near the Schiff bases
in bacteriorhodopsin and *Anabaena* sensory rhodopsin

Keisuke Saito [1], Hideki Kandori[2], and Hiroshi Ishikita [1, 3]*

[1] From 202 Building E, Career-Path Promotion Unit for Young Life Scientists, Graduate School of Medicine, Kyoto University, Yoshida-Konoe-cho, Sakyo-ku, Kyoto 606-8501, Japan

[2] Department of Frontier Materials, Nagoya Institute of Technology, Showa-ku, Nagoya 466-8555, Japan

[3] Japan Science and Technology Agency (JST), PRESTO, 4-1-8 Honcho Kawaguchi, Saitama 332-0012, Japan

Running Title: H-bond strength of water in BR and ASR

To whom correspondence should be addressed: Hiroshi Ishikita, 202 Building E, Career-Path Promotion Unit for Young Life Scientists, Graduate School of Medicine, Kyoto University, Yoshida-Konoe-cho, Sakyo-ku, Kyoto 606-8501, Japan, Tel. +81-75-753-9286, Fax. +81-75-753-9286, E-mail**: hiro@cp.kyoto-u.ac.jp

Background: Bacteriorhodopsin (BR) functions as a proton pump whereas Anabaena sensory rhodopsin (ASR) function as a photosensor.

Results: pK_a of the conserved Asp residues near the Schiff base significantly differ between BR and ASR.

Conclusion: The O-D stretching frequencies for D$_2$O is correlated with pK_a(Asp).

Significance: The presence of a strongly H-bonded water results from the proton-pumping activity in BR.

SUMMARY

Bacteriorhodopsin (BR) functions as a light-driven proton pump, whereas *Anabaena* sensory rhodopsin (ASR) is believed to function as a photosensor, despite the high similarity in their protein sequences. In Fourier transform infrared (FTIR) spectroscopic studies, the lowest O-D stretch for D$_2$O was observed at ~2200 cm^{-1} in BR but was significantly higher in ASR (>2500 cm^{-1}), which was previously attributed to a water molecule near the Schiff base (W402) that is H-bonded to Asp85 in BR and Asp75 in ASR. We investigated the factors that differentiate the lowest O-D stretches of W402 in BR and ASR. Quantum mechanical/molecular mechanical (QM/MM) calculations reproduced the H-bond geometries of the crystal structures and the calculated O-D stretching frequencies were corroborated by the FTIR band assignments. The potential-energy profiles indicate that the smaller O-D stretching frequency in BR originates from the significantly higher pK_a(Asp85) in BR relative to the pK_a(Asp75) in ASR, which were calculated to be 1.5 and –5.1, respectively. The difference is mostly due to the influences of Ala53, Arg82, Glu194-Glu204, and Asp212 on pK_a(Asp85) in BR, and the corresponding residues Ser47, Arg72, Ser188-Asp198, and Pro206 on pK_a(Asp75) in ASR. Because these residues participate in proton transfer pathways in BR but not in ASR, the presence of a strongly H-bonded water molecule near the Schiff base ultimately results from the proton-pumping activity in BR.

Bacteriorhodopsin (BR) functions as a light-driven proton pump and the driving force for its action is provided by photoisomerization of the all-*trans* retinal chromophore, which is covalently attached to Lys216 via the Schiff base, to 13-*cis*. This leads to proton transfer pathways that proceed toward the extracellular side via Asp96, the Schiff base, Asp85, and Glu204 (1-3). Asp 85 is located near the Schiff

1

base and serves as the counter ion. The presence of water molecules in this region had been suggested by Fourier transform infrared (FTIR) studies (4,5), and these were later confirmed as W401, W402, and W406 in the high-resolution crystal structure of the BR ground state (PDB code 1C3W; Figure 1) (6). The three water molecules form an H-bond network with Asp85, Arg82, Asp212, and the Schiff base. Among the three water molecules, the chemical properties of W402 are of particular interest because the water molecule is located at H-bond distances of 2.63 Å and 2.87 Å from the carboxyl O atom of Asp85 and the Schiff base N atom, respectively (Table 1). From FTIR analysis of various mutants in D_2O, the lowest O-D stretching frequency of 2171 cm^{-1} in BR was assigned to the $O_{W402}-H…O_{Asp85}$ bond, implying that this is the strongest H-bond in the network near the Schiff base (7). The band assignment presented in FTIR studies was also supported by previous computational studies by Hayashi and coworkers (8,9).

Water molecule W402 was also found in the crystal structure of *Anabaena* sensory rhodopsin (ASR) (PDB code 1XIO; Figure 1) (10). In contrast to the proton pumping of BR, ASR is believed to function as a photosensor. Despite the high similarity of their protein sequences, some key residues that are functionally important in the proton-pumping event in BR are not conserved in ASR: Asp96 in BR, which serves as a proton donor to the Schiff base, is replaced with Ser86 in ASR; Glu194 and Glu204 in BR, which is located in the terminal region of the proton transfer pathway, are replaced with Ser188 and Asp198, respectively. Although W402 is present in both BR (6) and ASR (10), Asp212 in BR is replaced with Pro206 in ASR (Figure 1). The absence of W401 and W406 in the corresponding H-bond network of ASR may be associated with the absence of an acidic residue corresponding to Asp212 in BR. FTIR studies have suggested that the O-D stretch in water molecules was only observed at >2500 cm^{-1} in ASR (11), which is ~300 cm^{-1} higher than the lowest O-D stretching frequency of 2171 cm^{-1} in BR (7).

The significant difference in the lowest O-D stretching frequency implies that the H-bond properties of W402 are significantly different in BR and ASR. It has been established by FTIR that the lowest O-D stretching frequency of water can be found at less than 2400 cm^{-1} in a number of proton-pumping rhodopsins (12). The same tendency also holds true for BR and ASR.

In the BR and ASR crystal structures, the angle defined by the Schiff base N, W402 O, and Asp85 O atoms ($N_{Lys}…O_{W402}…O_{Asp}$) differs significantly: the angle is $106°$ in BR (6) and $83°$ in ASR (10). Thus, it was proposed that the angle difference may

differentiate the H-bond strength of the water molecules in BR and ASR (11). On the other hand, it also appears that the $O_{W402}-H…O_{Asp}$ angle is more crucial than the $N_{Lys}…O_{W402}…O_{Asp}$ angle to the energetics of the H bond since it involves a H atom. In general, the $O_{donor}-H…O_{acceptor}$ angle strongly depends on the $O_{donor}-O_{acceptor}$ distance, i.e., the $O_{donor}-H…O_{acceptor}$ angle is more linear when the $O_{donor}-O_{acceptor}$ bond is shorter (13).

In addition, the $N_{Lys}…O_{W402}…O_{Asp}$ angle in the crystal structure can be directly altered in response to changes in the $O_{W402}-H…O_{Asp}$ distance. Because of the nature of H bonds (14-17), the $O_{W402}-H…O_{Asp85}$ distance could also be predominantly determined by the pK_a difference between the H-bond donor (W402) and acceptor (Asp) moieties. In general, a smaller pK_a difference yields a short, symmetrical H bond (14-17), and the H atom of $O_{W402}-H$ migrates toward the acceptor moiety, Asp. Unfortunately, the energetics of the $O_{W402}-H…O_{Asp}$ bond, particularly the pK_a difference between W402 and the Asp residue, remain unclear. Thus, it is essential to clarify how the $O_{W402}-H…O_{Asp}$ distance is energetically determined in the BR and ASR crystal structures.

Here, we present calculated O-D stretching frequencies of D_2O near W402 in BR and ASR in the ground state using a large-scale quantum mechanical/molecular mechanical (QM/MM) approach. We also present the potential-energy profiles of the H bond between W402 and Asp85 in BR, and W402 and Asp75 in ASR, and demonstrate that the frequencies and H-bond properties are ultimately determined predominantly by the pK_a values of H-bond acceptors Asp85 and Asp75. By calculating pK_a(Asp85) in BR and pK_a(Asp75) in ASR through solving the linear Poisson-Boltzmann equation with explicit consideration of the protonation states for all titratable residues, we are finally able to pinpoint the factors that cause a difference of ~300 cm^{-1} between the O-D stretching frequencies of W402 in BR and ASR.

EXPERIMENTAL PROCEDURES

As demonstrated in our previous work with photoactive yellow protein (18), we employed the following systematic modeling procedure.

First, we constructed initial molecular models of BR and ASR using their crystal structures and adding hydrogen atoms. Second, to gain better understanding of the electronic structure of W402 and the associated H-bond network, we performed large-scale QM/MM calculations for the entire BR and ASR proteins. To

gain insight into the QM/MM potential-energy profiles of the H bonds, O_{W402}–H…O_{Asp85} in BR and O_{W402}–H…O_{Asp75} in ASR, we calculated pK_a(Asp85) in BR and pK_a(Asp75) in ASR by simultaneously titrating all titratable residues in BR and ASR. Technical details of each modeling procedure are summarized below.

Atomic coordinates and charges. As a basis for the computations, the crystal structures of BR (PDB codes 1C3W (6) and 2NTU (19)) and ASR (PDB code 1XIO (10)) were used. To generate the initial geometries, the positions of the H atoms were energetically optimized with CHARMM (20) using the CHARMM22 force field. During this procedure, the positions of all non-H atoms were fixed and the standard charge states of all the titratable groups were maintained (i.e., basic and acidic groups were considered to be protonated and deprotonated, respectively). The Schiff base was considered to be protonated. Atomic partial charges of the amino acids and the Schiff base were adopted from the all-atom CHARMM22 (20) parameter set.

Protonation pattern and pK_a. The present computation is based on the electrostatic continuum model created by solving the linear Poisson-Boltzmann equation with the MEAD program (21). To facilitate a direct comparison with previous computational results (e.g., Refs. (22,23)), identical computational conditions and parameters, such as atomic partial charges and dielectric constants, were used. To obtain absolute pK_a values of target sites (e.g., pK_a(Asp85) of BR), we calculated the difference in electrostatic energy between the two protonation states, protonated and deprotonated, in a reference model system using a known experimentally measured pK_a value (e.g., 4.0 for Asp (24)). The difference in the pK_a value of the protein relative to the reference system was added to the known reference pK_a value. The experimentally measured pK_a values employed as references were 7.2 for the Schiff base (25,26), 12.0 for Arg, 4.0 for Asp, 9.5 for Cys, 4.4 for Glu, 10.4 for Lys, 9.6 for Tyr (24), and 7.0 and 6.6 for the $N\varepsilon$ and $N\delta$ atoms of His, respectively (27-29). All other titratable sites were fully equilibrated to the protonation state of the target site during the titration. The ensemble of the protonation patterns was sampled by a Monte Carlo (MC) method with Karlsberg (30). The dielectric constants were set to $\varepsilon_p = 4$ inside the protein and $\varepsilon_w = 80$ for water. All computations were performed at 300 K, pH 7.0, and an ionic strength of 100 mM. The linear Poisson-Boltzmann equation was solved using a three-step grid-focusing procedure at resolutions of 2.5 Å, 1.0 Å, and 0.3 Å. The MC sampling yielded the probabilities [protonated] and [deprotonated] of the

two protonation states of the molecule. The pK_a value was evaluated using the Henderson-Hasselbalch equation. A bias potential was applied to obtain an equal amount of both protonation states ([protonated] = [deprotonated]), yielding the pK_a value as the resulting bias potential.

QM/MM calculations. We employed an electrostatic embedding QM/MM scheme and used the Qsite (31) program code, as performed in previous studies (32). We employed the restricted DFT method with B3LYP functional and LACVP**+ basis sets. The geometries were refined using a constrained QM/MM optimization, whereby the coordinates of the heavy atoms in the surrounding MM region were fixed to the original X-ray coordinates, whereas those of the H atoms in the MM region were optimized with the OPLS-2005 force field. To investigate the energetics of the entire H-bond network, the QM region was defined as follows (Figure 2): (a) W402 and the residues/groups in the same H-bond network, i.e., W401, W406, Tyr57, Arg82, Asp85, Ser85, Thr89, Tyr185, Asp212, Lys216 (the Schiff base), and retinal for BR; and (b) W402, and the residues/groups in the same H-bond network, i.e., Tyr11, Tyr51, Asp75, Trp76, Thr79, Ser47, the backbone of Phe202, Lys210 (the Schiff base), and retinal for ASR. Other residues that are not in the H-bond network of W402 (e.g., Trp86 in BR is not involved in the same H-bond network, even though the residue corresponds to Trp76 in ASR) were approximated by the MM force field. The resulting QM/MM optimized geometries are listed in Table S1 in the SI. The potential-energy profile of the H bond was obtained in the following manner: first, we optimized the geometry without constraints using QM/MM and used the resulting geometry as the initial geometry for the subsequent steps. Next, we moved the H atom from the H-bond donor atom (O_{donor}) to the acceptor atom ($O_{acceptor}$) by 0.05 Å, optimized the geometry by constraining the O_{donor}–H and $O_{acceptor}$…H distances, and then calculated the energy of the resulting geometry. This procedure was repeated until the H atom reached the $O_{acceptor}$ atom. After obtaining the stable geometry of the QM fragment, we calculated the O-D stretching frequencies of W401, W402, and W406 in BR, and of W402 in ASR. The frequency calculations were performed using a numerical differentiation method at the same level as the QM/MM geometry optimization. The calculated frequencies were scaled using a standard factor of 0.9614 for B3LYP (33).

Calculation of the O-D stretching frequencies of D_2O from an empirical equation. The O-D stretching frequencies of D_2O were also evaluated on the basis of the resultant QM/MM optimized geometries by using the correlation of stretching frequency with respect to bond distance of the O_{donor}–

D…$O_{acceptor}$ bond, as previously proposed by Mikenda (34). This correlation was empirically expressed with the O-D stretching frequency, ν_{O-D}, and the O_{donor}–$O_{acceptor}$ bond distance, r_{O-O}, by

$$\nu_{O-D} \ [\text{cm}^{-1}] = 2727 - A \exp(-B \ r_{O-O} \ [\text{Å}]),$$
    (eq. 1)

where $A = 2.11 \times 10^6$ and $B = 3.23$ for the O_{water}–D_{water}…$O_{acceptor}$ bond (34). Note that these parameters were derived from spectroscopic and X-ray diffraction data for 61 different solid deuterates, e.g., $CaSO_4 \cdot 2D_2O$ and $MnCl_2 \cdot 6D_2O$ (34).

To predict the frequencies, eq. 1 requires only the O_{donor}–$O_{acceptor}$ distance, which can be preferentially taken from the QM/MM optimized geometry. Remarkably, the O-D stretching frequencies calculated by a QM/MM numerical differentiation method were reasonably well-reproduced using eq. 1 solely from the optimized O_{donor}–$O_{acceptor}$ distance, particularly for frequencies <2500 cm^{-1} (Table 2b).

Notably, eq. 1 indicates that the O-D stretching frequency of 2500 cm^{-1} corresponds to the $O_{acceptor}$–O_{donor} distance of ~2.8 Å. The deviation from the values calculated with the QM/MM numerical differentiation method appears to be more pronounced for frequencies >2500 cm^{-1} (Figure 3). Because the original parameters were derived from solid hydrates (34), the larger deviation for weak H bonds at these frequencies may be due to H-bond patterns or mode couplings specific to the protein environments.

RESULTS

H-bond geometries near W402 in BR. The O-D stretching frequencies of D_2O predominantly depend on the H-bond geometry, particularly the H bond donor-acceptor distance (O_{donor}–$O_{acceptor}$) (34). If the assumed H-bond pattern is not correct, the resulting QM/MM optimized geometries significantly deviate from the original crystal structure. Thus, although the QM/MM optimized geometries (especially the heavy atom positions) are not always consistent with the crystal structures, it is necessary to carefully evaluate the H-bond pattern with respect to the atomic coordinates of the crystal structures prior to frequency calculations.

In BR, two H-bond patterns are geometrically possible for the H-bond network of W402 (Figure 4). A model previously presented from FTIR studies (7) suggests that an H atom of W401 has no H-bond acceptor (model 1), while an alternative model suggests that an H atom of W406 has no H-bond acceptor (model 2). The QM/MM optimized geometries of the two models appear to represent the actual H bond patterns of the crystal structures because of the low RMSD (0.17–0.19 Å, Table 1), implying that the two models probably coexist as tautomers in the actual BR protein environment.

Model 1 resembles the QM/MM geometry reported by Hayashi and Ohmine (8). However, in their QM/MM geometry, the O_{W402}–O_{Asp212} distance was significantly elongated to 4.07 Å and the H bond is absent (8). This varies significantly from the crystal structures and the present QM/MM geometries (O_{W402}–O_{Asp212} = 2.85–3.01 Å, Table 2). In the reported QM/MM geometry, W402 forms a new H bond with another carboxyl O atom of Asp212 (Figure 4). Hence, it is to be considered that the band assignment reported by Hayashi and Ohmine (8) refers to another possible H-bond geometry that differs from the crystal structures.

The QM/MM geometries imply that model 1 can explain the O_{donor}–$O_{acceptor}$ distances in the crystal structure provided by Luecke et al. (PDB code 1C3W) (6) more reasonably than model 2 (Table 1). On the other hand, model 2 appears to explain the O_{donor}–$O_{acceptor}$ distances in the crystal structure determined by Lanyi et al. (PDB code 2NTU) (19) more reasonably, namely in terms of O_{W402}–O_{Asp85}, O_{W402}–O_{Asp212}, O_{W401}–O_{Asp85}, and O_{Arg82}–O_{W406} distances(Table 1). However, the small discrepancies could also be due to being artifacts of the crystallization process. Because the resolutions of the two crystal structures are 1.53 and 1.55 Å (which are essentially the same), both of the H-bond tautomers are likely to contribute to the O-D stretching frequencies measured by FTIR. If both tautomers are present, this might corroborate the rapid H/D exchange observed in this region.

Calculated O-D stretching frequencies in BR. In FTIR studies (7), the three H bonds O_{W401}–H…O_{Asp85}, O_{W402}–H…O_{Asp85}, and O_{W406}–H…O_{Asp212} were classified as being strong H bonds because of the assignment of low frequencies (Figure 4).

a) Model 1. In FTIR studies (7), the lowest frequency of 2171 cm^{-1} was assigned to O_{W402}–H…O_{Asp85}. However, in model 1, O_{W402}–H…O_{Asp85} was longer than O_{W401}–H…O_{Asp85} (Table 1), leading to a larger calculated O-D stretching frequency for O_{W402}–H…O_{Asp85} than O_{W401}–H…O_{Asp85} (Table 2a), as predicted from the empirical equation by Mikenda (eq. 1) (34).

In model 1, two mode couplings between O_{W401}–H…O_{Asp85} and O_{W401}–H…O_{Asp85}, and between O_{W406}–H…O_{Asp212} and O_{W406}–H…O_{W401} were observed. However, the latter coupling is not consistent with the FTIR assignments. In FTIR studies, H bonds O_{W406}–

4

H…O_{Asp212} and O_{W406}–H…O_{W401} were assigned as strong (2292 cm^{-1}) and weak (2599 cm^{-1}), respectively (Table 2a) (7). Because mode couplings are unlikely to occur between a strong and weak H bond, model 1 fails to sufficiently explain the FTIR assignments.

b) Model 2. In contrast to model 1, model 2 can reasonably explain the strong H bond (2292 cm^{-1}) of O_{W406}–H…O_{Asp212} and the weak H bond (2636 cm^{-1}) of O_{W406}–H…O_{W401} that were assigned by FTIR studies (Table 2b). Furthermore, the lowest calculated frequency was observed for O_{W402}–H…O_{Asp85}, which is also consistent with FTIR studies (7). Significantly high correlations of the frequencies predicted from eq. 1 suggest that assignment of the O-D stretching frequencies on the basis of model 2 is also justified by the H-bond geometry. Note that no remarkable mode couplings were observed for model 2 in the QM/MM calculations.

In the following section, further analysis of BR will be discussed on the basis of model 2 using the crystal structure by Luecke et al. (PDB code 1C3W) (6) unless otherwise specified.

H-bond geometries near W402 and O-D stretching frequencies in ASR. In contrast to BR, the ASR crystal structure only possesses a single water molecule, W402, near the Schiff base (Figure 4). The H-bond geometry of the crystal structure was reasonably reproduced by the QM/MM geometry optimization (Table 3). In the QM/MM calculations, the lowest O-D stretching frequency of 2376 cm^{-1} in ASR, which was found for O_{W402}–H…O_{Asp75} (Table 4), was significantly larger (by ~300 cm^{-1}) than that for the corresponding O_{W402}–H…O_{Asp85} in BR (2078 cm^{-1}, Table 2b). In FTIR studies, the O-D stretching of D_2O was only observed in the >2500 cm^{-1} region for ASR (11), which was also ~300 cm^{-1} higher than the lowest frequency of 2171 cm^{-1} in BR (7). Since the main purpose of the present study is to understand the reason for the significant discrepancy between the lowest frequencies of D_2O (assumed as W402 (11)) of BR and ASR, these computational results are sufficiently accurate for our purpose to describe the chemical properties of W402.

DISCUSSION

Understanding frequencies from energetics.

Significant differences between the H-bond energy profiles of BR and ASR. To identify the origin of the difference in O-D stretching frequencies of W402, we analyzed the potential-energy profiles of H-bonds O_{W402}–H…O_{Asp85} in BR and O_{W402}–H…O_{Asp75} in ASR by altering the H atom position

along the O_{W402}–$O_{Asp85/75}$ bond (Figure 5). In both H bonds, the energy minimum was found at the W402 moiety rather than at the Asp moiety, suggesting that in the ground state, W402 exists as H_2O in the presence of deprotonated Asp in BR and ASR.

On the other hand, the potential-energy profiles of the Asp moiety were significantly different for BR and ASR. For an H atom along the O_{W402}–$O_{Asp85/75}$ bond, the energy of the Asp85 moiety of BR is significantly lower than that of the Asp75 moiety of ASR. Thus, it is more favorable for an H atom of O_{W402}–H to be at the Asp moiety in BR than in ASR, indicating that pK_a(Asp) is significantly higher for BR than ASR (arrow 1 in Figure 5). As clearly shown in Figure 5, the lower energy near the Asp85 moiety in BR leads to greater broadening of the potential-well width near W402 toward Asp85, which corresponds to an elongation of O_{W402}–H. Thus, the H atom of O_{W402}–H migrates toward the H-bond acceptor Asp more in BR than in ASR (arrow 2 in Figure 5). It should be noted that the longer O_{W402}–H corresponds to a smaller O-D stretching frequency. It is also obvious from the width of the entire well of the potential-energy profiles that the O_{W402}–O_{Asp85} length in BR (~2.6 Å, Table 1), which is shorter than the O_{W402}–O_{Asp75} length in ASR (~2.7 Å, Table 3), is a result of the smaller pK_a difference between W402 and the Asp residue in BR relative to the corresponding difference in ASR (arrow 3 in Figure 5).

Thus, from the potential-energy profiles (Figure 5), the difference of ~300 cm^{-1} in the O-D stretching frequency is mainly due to the difference between the pK_a values for the Asp residues in BR and ASR.

pK_a(Asp85) in BR and pK_a(Asp75) in ASR

Factors that differentiate pK_a(Asp) of BR and ASR. By solving the linear Poisson–Boltzmann equation, we calculated pK_a(Asp85) in BR and pK_a(Asp75) in ASR to be 1.5 and −5.1, respectively, in the presence of the protonated Schiff base (Table 5). The calculated pK_a(Asp85) of 1.5 is consistent with an experimentally measured pK_a(Asp85) of 2.2–2.6 in the presence of the protonated Schiff base (2,35). Although pK_a(Asp75) is not known, the significantly low pK_a(Asp85) in BR relative to pK_a(Asp75) in ASR is consistent with the QM/MM-calculated potential-energy profiles (Figure 5). The significantly low pK_a(Asp75) in ASR appears to be consistent with the fact that Asp75 remains deprotonated throughout the photocycle (36).

a) Asp212 in BR. The most significant difference observed between pK_a(Asp85) and pK_a(Asp75) was induced by the substitution of Asp212 in BR for Pro206 in ASR (Figure 6), which is responsible for the pK_a difference of ~6 (Table 5). Because Asp212 is an H-bond acceptor for O_{W402}–H and is thus far the most proximal negative charge to Asp85 (5.1 Å), Asp212 upshifts pK_a(Asp85) by the largest amount among all residues in BR (Table 5).

It is widely known that both Asp85 and Asp212 are ionized in the ground state (2,37,38). However, the deprotonated state of Asp212 is more energetically stable than the deprotonated state of Asp85, as seen in the lower pK_a(Asp212) of –2.0 (Table 6); this is consistent with previous pK_a assignments of <1 for Asp212 (39,40) or pK_a(Asp85) < pK_a(Asp212) (41,42). The deprotonated state of Asp212 was facilitated by H-bond donations from Tyr57 (decreasing pK_a(Asp212) by 3.4) and Tyr185 (decreasing pK_a(Asp212) by 3.3). In addition, Arg82 is closer to Asp212 (3.8 Å) than Asp85 (6.6 Å) (Figure 6), stabilizing the ionized state of Asp212 more effectively than Asp85 (increasing pK_a by ~ 6, Table 6).

Although the most significant difference between pK_a(Asp85) and pK_a(Asp75) induced by the substitution of Asp212 in BR for Pro206 in ASR is remarkable, this is not sufficient to entirely explain the difference between pK_a(Asp85) and pK_a(Asp75) (see below), which is in agreement with mutational studies of ASR mutant P206D (43).

b) Ser47 in ASR. Ser47 donates an H bond to Asp75 in ASR, decreasing pK_a(Asp75) by 3.2, whereas the corresponding residue in BR is the non-polar Ala53 (Table 5). This was responsible for a pK_a difference of 2.7 between Asp85 and Asp75 (Table 5).

c) Glu194-Glu204 pair in BR. Another remarkable pK_a(Asp85) upshift in BR originates from the Glu194-Glu204 moiety near the terminal region of the proton transfer pathway (2,3) (Figure 6). It is likely that the two acidic residues share a proton. The corresponding acidic residue pair is absent in ASR, thereby contributing slightly to the larger pK_a(Asp) in BR relative to that in ASR (~0.5 pK_a units, Table 5). In the present study, Glu204 is protonated and Glu194 is deprotonated when Ser193 donates an H bond to Glu194, which is consistent with the previously reported pK_a(Glu204) of ~9 (35,44,45).

Nevertheless, the geometry of the crystal structure also suggests that protonated Glu194 and deprotonated Glu204 are almost equally possible when Ser193 donates an H bond to Glu204, as suggested by Gerwert et al. (46). Thus, it would be

more plausible to consider the two acidic residues as a pair that possesses ~1 H^+ as concluded in previous QM/MM simulations (47). This resembles a pair of acidic residues, Glu-L212 and Asp-L213, in the proton transfer pathway of photosynthetic reaction centers, which has been interpreted as sharing ~1 H^+ (48-50). Deprotonated Glu194 contributes to an increase in pK_a(Asp85) of ~1 (Table 5); this therefore corroborates the linkage between pK_a(Asp85) and pK_a(Glu204) previously reported in mutant BR studies (35) if we consider Glu194-Glu204 as a pair of acidic residues sharing ~1 H^+.

d) Orientation of Arg82 in BR and Arg72 ASR. Arg82 was found to contribute to an increase in pK_a(Asp85) of 3.1 in BR (Table 5), which is in agreement with a similar increase (~4.5) reported for BR mutants R82Q and R82A (51,52). Irrespective of the conservation of Arg82/Arg72 in BR/ASR, their influence on pK_a(Asp85) and pK_a(Asp75) significantly differ by ~2 because the side chain of Arg72 is oriented away from the Schiff base and toward the extracellular side in ASR (O_{Asp75}–N_{Arg72} = 9.6 Å) (10), which is the opposite of the orientation of Arg82 in BR (O_{Asp85}–N_{Arg82} = 6.6 Å) (6) (Figure 6). Thus, the differing orientations of the Arg side chains decrease the pK_a(Asp) difference between BR and ASR (Table 6).

In summary, the significantly large pK_a(Asp85) in BR relative to pK_a(Asp75) in ASR is largely due to the presence of Asp212 near Asp85 in BR and the absence of the corresponding acidic residue in ASR. In addition, the donation of an H-bond from Ser47 to Asp75 lowers the pK_a(Asp75) in ASR by facilitating deprotonation. The corresponding polar residue is absent in BR; this upshifts pK_a(Asp85) in BR relative to pK_a(Asp75) in ASR. The Glu194-Glu204 pair is located near the terminal region of the proton transfer pathway in BR, whereas only a single acidic residue is located near the corresponding position in ASR. This also upshifts pK_a(Asp85) in BR relative to pK_a(Asp75) in ASR.

CONCLUSIONS

QM/MM calculations revealed that the heavy atom positions in the BR crystal structures could be explained by one of two models. Model 2 can reasonably explain the strong H bond (2292 cm^{-1}) of O_{W406}–H…O_{Asp212} and the weak H bond (2636 cm^{-1}) of O_{W406}–H…O_{W401}, as previously assigned by FTIR (Table 2b). In model 2, the lowest calculated frequency was observed at O_{W402}–H…O_{Asp85}, which is also consistent with FTIR studies. Essentially the same frequencies were also predicted solely from the

6

$O_{donor}–O_{acceptor}$ distances using eq. 1 proposed by Mikenda (34). This suggests that eq. 1 can be used to support the frequency assignments made from spectroscopic studies. In ASR, the lowest calculated O-D stretching frequency is observed at $O_{W402}–H…O_{Asp75}$, which is ~300 cm^{-1} higher than that of BR (Tables 2b and 4), as previously reported in FTIR studies of BR (7) and ASR (11).

The potential-energy profiles of two H bonds, $O_{W402}–H…O_{Asp85}$ in BR and $O_{W402}–H…O_{Asp75}$ in ASR, demonstrate that the significant pK_a difference between Asp85 in BR and Asp75 in ASR is ultimately responsible for the difference of ~300 cm^{-1} in the O-D stretching frequency of W402 between BR and ASR (Figure 5). Electrostatic calculations resulted in a $pK_a(Asp85)$ of 1.5 in BR and a $pK_a(Asp75)$ of −5.1 in ASR (Table 5). The pK_a difference is mainly due to differences in the influences of Ala53, Arg82, Glu194, and Asp212 on Asp85 in BR, and the corresponding residues Ser47, Arg72, Ser188, and Pro206 on Asp75 in ASR, indicating the presence of long-range electrostatic interactions along the proton transfer pathways (53). A strongly H-bonded water near the Schiff base, which results from electrostatic interactions between Asp85 and these acidic residues in BR, could play a key role in proton transfer.

REFERENCES

1. Lanyi, J. K. (1998) Understanding structure and function in the light-driven proton pump bacteriorhodopsin. *J Struct Biol* **124**, 164-178
2. Balashov, S. P. (2000) Protonation reactions and their coupling in bacteriorhodopsin. *Biochim Biophys Acta* **1460**, 75-94
3. Kandori, H. (2000) Role of internal water molecules in bacteriorhodopsin. *Biochim Biophys Acta* **1460**, 177-191
4. Maeda, A., Sasaki, J., Yamazaki, Y., Needleman, R., and Lanyi, J. K. (1994) Interaction of aspartate-85 with a water molecule and the protonated Schiff base in the L intermediate of bacteriorhodopsin: a Fourier-transform infrared spectroscopic study. *Biochemistry* **33**, 1713-1717
5. Kandori, H., Yamazaki, Y., Sasaki, J., Needleman, R., Lanyi, J. K., and Maeda, A. (1995) Water-mediated proton transfer in proteins: an FTIR study of bacteriorhodopsin. *J Am Chem Soc* **117**, 2118-2119
6. Luecke, H., Schobert, B., Richter, H. T., Cartailler, J. P., and Lanyi, J. K. (1999) Structure of bacteriorhodopsin at 1.55 A resolution. *J Mol Biol* **291**, 899-911
7. Shibata, M., and Kandori, H. (2005) FTIR studies of internal water molecules in the Schiff base region of bacteriorhodopsin. *Biochemistry* **44**, 7406-7413
8. Hayashi, S., and Ohmine, I. (2000) Proton transfer in bacteriorhodopsin: structure, excitation, IR spectra, and potential energy surface analyses by an ab initio QM/MM method. *J Phys Chem B* **104**, 10678-10691
9. Hayashi, S., Tajkhorshid, E., Kandori, H., and Schulten, K. (2004) Role of hydrogen-bond network in energy storage of bacteriorhodopsin's light-driven proton pump revealed by ab initio normal-mode analysis. *J Am Chem Soc* **126**, 10516-10517
10. Vogeley, L., Sineshchekov, O. A., Trivedi, V. D., Sasaki, J., Spudich, J. L., and Luecke, H. (2004) Anabaena sensory rhodopsin: a photochromic color sensor at 2.0 A. *Science* **306**, 1390-1393
11. Furutani, Y., Kawanabe, A., Jung, K. H., and Kandori, H. (2005) FTIR spectroscopy of the all-trans form of Anabaena sensory rhodopsin at 77 K: hydrogen bond of a water between the Schiff base and Asp75. *Biochemistry* **44**, 12287-12296
12. Kandori, H. (2010) in Hydrogen bonds of protein-bound water molecules in rhodopsins, In Hydrogen bonding and transfer in the excited state (Han, K.-L. and Zhao, G.-J., Eds). pp 377-391, John-Wiley & Sons Ltd., West Sussex
13. Frey, P. A. (2006) *in Isotope Effects in Chemistry and Biology (Kohen, A. and Limbach, H.-H., Eds.)*, pp 975-993, CRC press, Boca Raton, FL
14. Cleland, W. W., and Kreevoy, M. M. (1994) Low-barrier hydrogen bonds and enzymic catalysis. *Science* **264**, 1887-1890

15. Frey, P. A., Whitt, S. A., and Tobin, J. B. (1994) A low-barrier hydrogen bond in the catalytic triad of serine proteases. *Science* **264**, 1927-1930

16. Perrin, C. L., and Nielson, J. B. (1997) "Strong" hydrogen bonds in chemistry and biology. *Annu Rev Phys Chem* **48**, 511-544

17. Schutz, C. N., and Warshel, A. (2004) The low barrier hydrogen bond (LBHB) proposal revisited: the case of the Asp... His pair in serine proteases. *Proteins* **55**, 711-723

18. Saito, K., and Ishikita, H. (2012) Energetics of short hydrogen bonds in photoactive yellow protein. *Proc Natl Acad Sci U S A* **109**, 167-172

19. Lanyi, J. K., and Schobert, B. (2007) Structural changes in the L photointermediate of bacteriorhodopsin. *J Mol Biol* **365**, 1379-1392

20. Brooks, B. R., Bruccoleri, R. E., Olafson, B. D., States, D. J., Swaminathan, S., and Karplus, M. (1983) CHARMM: a program for macromolecular energy minimization and dynamics calculations. *J. Comput. Chem.* **4**, 187-217

21. Bashford, D., and Karplus, M. (1990) pK_a's of ionizable groups in proteins: atomic detail from a continuum electrostatic model. *Biochemistry* **29**, 10219-10225

22. Ishikita, H., and Knapp, E.-W. (2007) Protonation states of ammonia/ammonium in the hydrophobic pore of ammonia transporter protein AmtB. *J. Am. Chem. Soc.* **129**, 1210-1215

23. Ishikita, H. (2010) Origin of the pK_a shift of the catalytic lysine in acetoacetate decarboxylase. *FEBS Lett* **584**, 3464-3468

24. Nozaki, Y., and Tanford, C. (1967) Acid-base titrations in concentrated guanidine hydrochloride. Dissociation constants of the guamidinium ion and of some amino acids. *J Am Chem Soc* **89**, 736-742

25. Bassov, T., and Sheves, M. (1986) Alteration of pK_a of the bacteriorhodopsin protonated Schiff base. A study with model compounds. *Biochemistry* **25**, 5249-5258

26. Rousso, I., Friedman, N., Sheves, M., and Ottolenghi, M. (1995) pK_a of the protonated Schiff base and aspartic 85 in the bacteriorhodopsin binding site is controlled by a specific geometry between the two residues. *Biochemistry* **34**, 12059-12065

27. Tanokura, M. (1983) 1H-NMR study on the tautomerism of the imidazole ring of histidine residues. I. Microscopic pK values and molar ratios of tautomers in histidine-containing peptides. *Biochim Biophys Acta* **742**, 576-585

28. Tanokura, M. (1983) 1H-NMR study on the tautomerism of the imidazole ring of histidine residues. II. Microenvironments of histidine-12 and histidine-119 of bovine pancreatic ribonuclease A. *Biochim Biophys Acta* **742**, 586-596

29. Tanokura, M. (1983) 1H nuclear magnetic resonance titration curves and microenvironments of aromatic residues in bovine pancreatic ribonuclease A. *J Biochem* **94**, 51-62

30. Rabenstein, B., and Knapp, E. W. (2001) Calculated pH-dependent population and protonation of carbon-monoxy-myoglobin conformers. *Biophys J* **80**, 1141-1150

31. QSite, version 5.6, Schrödinger, LLC, New York, NY, 2010.

32. Saito, K., Ishida, T., Sugiura, M., Kawakami, K., Umena, Y., Kamiya, N., Shen, J.-R., and Ishikita, H. (2011) Distribution of the cationic state over the chlorophyll pair of photosystem II reaction center. *J. Am. Chem. Soc.* **133**, 14379-14388

33. Scott, A. P., and Radom, L. (1996) Harmonic vibrational frequencies: an evaluation of Hartree−Fock, Møller−Plesset, quadratic configuration interaction, density functional theory, and semiempirical scale factors. *J Phys Chem* **100**, 16502-16513

34. Mikenda, W. (1986) Stretching frequency versus bond distance correlation of O-D(H)...Y (Y = N, O, S, Se, Cl, Br, I) hydrogen bonds in solid hydrates. *J Mol Struct* **147**, 1-15

35. Richter, H. T., Brown, L. S., Needleman, R., and Lanyi, J. K. (1996) A linkage of the pK_a's of asp-85 and glu-204 forms part of the reprotonation switch of bacteriorhodopsin. *Biochemistry* **35**, 4054-4062

36. Bergo, V. B., Ntefidou, M., Trivedi, V. D., Amsden, J. J., Kralj, J. M., Rothschild, K. J., and Spudich, J. L. (2006) Conformational changes in the photocycle of Anabaena sensory rhodopsin: absence of the Schiff base counterion protonation signal. *J Biol Chem* **281**, 15208-15214

37. Song, Y., Mao, J., and Gunner, M. R. (2003) Calculation of proton transfers in Bacteriorhodopsin bR and M intermediates. *Biochemistry* **42**, 9875-9888

38. Bombarda, E., Becker, T., and Ullmann, G. M. (2006) Influence of the membrane potential on the protonation of bacteriorhodopsin: insights from electrostatic calculations into the regulation of proton pumping. *J Am Chem Soc* **128**, 12129-12139

39. Metz, G., Siebert, F., and Engelhard, M. (1992) Asp85 is the only internal aspartic acid that gets protonated in the M intermediate and the purple-to-blue transition of bacteriorhodopsin. A solid-state 13C CP-MAS NMR investigation. *FEBS Lett* **303**, 237-241

40. Balashov, S. P., Govindjee, R., Imasheva, E. S., Misra, S., Ebrey, T. G., Feng, Y., Crouch, R. K., and Menick, D. R. (1995) The two pKa's of aspartate-85 and control of thermal isomerization and proton release in the arginine-82 to lysine mutant of bacteriorhodopsin. *Biochemistry* **34**, 8820-8834

41. Bashford, D., and Gerwert, K. (1992) Electrostatic calculations of the pKa values of ionizable groups in bacteriorhodopsin. *J Mol Biol* **224**, 473-486

42. Sampogna, R. V., and Honig, B. (1994) Environmental effects on the protonation states of active site residues in bacteriorhodopsin. *Biophys J* **66**, 1341-1352

43. Choi, A. R., Kim, S. Y., Yoon, S. R., Bae, K., and Jung, K. H. (2007) Substitution of Pro206 and Ser86 residues in the retinal binding pocket of Anabaena sensory rhodopsin is not sufficient for proton pumping function. *J Microbiol Biotechnol* **17**, 138-145

44. Balashov, S. P., Imasheva, E. S., Govindjee, R., and Ebrey, T. G. (1996) Titration of aspartate-85 in bacteriorhodopsin: what it says about chromophore isomerization and proton release. *Biophys J* **70**, 473-481

45. Dioumaev, A. K., Richter, H. T., Brown, L. S., Tanio, M., Tuzi, S., Saito, H., Kimura, Y., Needleman, R., and Lanyi, J. K. (1998) Existence of a proton transfer chain in bacteriorhodopsin: participation of Glu-194 in the release of protons to the extracellular surface. *Biochemistry* **37**, 2496-2506

46. Rammelsberg, R., Huhn, G., Lubben, M., and Gerwert, K. (1998) Bacteriorhodopsin's intramolecular proton-release pathway consists of a hydrogen-bonded network. *Biochemistry* **37**, 5001-5009

47. Goyal, P., Ghosh, N., Phatak, P., Clemens, M., Gaus, M., Elstner, M., and Cui, Q. (2011) Proton storage site in bacteriorhodopsin: new insights from quantum mechanics/molecular mechanics simulations of microscopic pK_a and infrared spectra. *J Am Chem Soc* **133**, 14981-14997

48. Alexov, E. G., and Gunner, M. R. (1999) Calculated protein and proton motions coupled to electron transfer: electron transfer from Q_A^- to Q_B in bacterial photosynthetic reaction centers. *Biochemistry* **38**, 8253-8270

49. Gerencser, L., and Maroti, P. (2001) Retardation of proton transfer caused by binding of the transition metal ion to the bacterial reaction center is due to pK_a shifts of key protonatable residues. *Biochemistry* **40**, 1850-1860

50. Ishikita, H., Morra, G., and Knapp, E.-W. (2003) Redox potential of quinones in photosynthetic reaction centers from *Rhodobacter sphaeroides*: dependence on protonation of Glu-L212 and Asp-L213. *Biochemistry* **42**, 3882-3892

51. Otto, H., Marti, T., Holz, M., Mogi, T., Stern, L. J., Engel, F., Khorana, H. G., and Heyn, M. P. (1990) Substitution of amino acids Asp-85, Asp-212, and Arg-82 in bacteriorhodopsin affects the proton release phase of the pump and the pK of the Schiff base. *Proc Natl Acad Sci U S A* **87**, 1018-1022

52. Brown, L. S., Bonet, L., Needleman, R., and Lanyi, J. K. (1993) Estimated acid dissociation constants of the Schiff base, Asp-85, and Arg-82 during the bacteriorhodopsin photocycle. *Biophys J* **65**, 124-130

53. Calimet, N., and Ullmann, G. M. (2004) The influence of a transmembrane pH gradient on protonation probabilities of bacteriorhodopsin: the structural basis of the back-pressure effect. *J Mol Biol* **339**, 571-589

FOOTNOTES

FIGURE LEGENDS

Figure 1. Overview of the BR (PDB code 1C3W) and ASR (PDB code 1XIO) structures. Red spheres indicate O atoms of water molecules. Yellow arrows indicate proton transfer pathways.

Figure 2. Residues and groups included in the QM regions for (a) BR and (b) ASR. Dotted lines indicate hydrogen bonds. (c) Geometry of moieties near Lys210 in ASR before (magenta) and after (yellow) the QM/MM optimization.

Figure 3. The geometric correlation of the O-D stretching frequencies with the $O_{acceptor} \cdots H–O_{donor}$ bond of H_2O (correlation with the $O_{donor}–O_{acceptor}$ distance). Each □ represents the $O_{donor}–O_{acceptor}$ distance of the QM/MM optimized geometries (Tables 1 and 3) and the O-D stretching frequency calculated by a QM/MM numerical differentiation method (Tables 2 and 4). The solid curve was determined using an empirical equation (eq. 1) proposed by Mikenda (34).

Figure 4. H-bond geometries of water molecules near the Schiff base in BR and ASR. Pink arrows in model 1 indicate mode couplings of the two O-D bonds. Red dotted lines indicate "strong H bonds" reported in FTIR studies (7).

Figure 5. Potential-energy profiles along the proton transfer coordinates of $O_{W402}–H \ldots O_{Asp85}$ in BR (black solid line) and $O_{W402}–H \ldots O_{Asp75}$ in ASR (blue solid line). ΔE describes the difference in energy relative to the energy minimum. Boxed arrows indicate the shifts in the potential energy curve accompanied by the $pK_a(Asp)$ change from ASR to BR. The marginal energy drop near 1.74 Å in $O_{W402}–H$ of ASR was due to an alteration of the H-bond pattern; below 1.74 Å, Ser47 donates an H bond to the carboxyl O atom of Asp75, which is simultaneously H-bonded by W402. At 1.74 Å, the hydroxyl H atom is oriented toward another carboxyl O atom of Asp75 due to the unusual proximity of the H atom of W402 to Asp75.

Figure 6. Residues that contribute to differences between $pK_a(Asp)$ of (a) BR and (b) ASR.

Table 1. Comparison of the H-bond geometries near W402 in the BR crystal structures (PDB ID codes 1C3W at 1.55 Å resolution and 2NTU at 1.53 Å resolution), in the QM/MM geometry by Hayashi and Ohmine (8), and in the present study (models 1 and 2, Figure 4). Distances in Å, angles in °. n.d. = not determined. An underlined number indicates a significant deviation from the distance in the crystal structure. See Table S1 in the SI for the atomic coordinates of the QM/MM geometries.

Donor…acceptor	1C3W	QM/MM Hayashi & Ohmine[a] (model 1)	QM/MM (model 1)	QM/MM (model 2)	2NTU	QM/MM (model 1)	QM/MM (model 2)
W402…Asp85	2.63	2.58	2.61	2.57	2.52	2.63	2.59
W402…Asp212	2.85	<u>4.07</u>	2.92	2.99	3.01	2.90	2.95
W401…Asp85	2.59	2.63	2.51	2.64	2.69	2.59	2.68
(OH without acceptor) [b]		(W401)	(W401)	(W406)		(W401)	(W406)
W406…W401	2.75	2.77	2.76	3.06	2.69	2.78	3.07
W406…Asp212	2.75	2.78	2.64	2.64	2.81	2.73	2.65
Lys216…W402	2.87	2.63	2.78	2.76	2.94	2.80	2.77
Arg82…W406	2.49	2.72	2.74	2.87	2.87	2.73	2.86
RMSD	n. d.	n. d.	0.19	0.18	n. d.	0.17	0.18
angle(N_{Lys216}…O_{W402}…O_{Asp85})	106	n. d.	108	108	111	111	111

[a] See Ref. (8).

[b] A water molecule in which one of the two O-H bonds does not possess the H-bond acceptor molecule; W401 in model 1 and W402 in model 2 (Figure 4).

Table 2. O–D stretching frequencies (in cm^{-1}) of the water molecules near W402 in BR. Connecting lines indicate the presence of coupling between the two modes. n.d. = not determined. R^2 = correlation coefficient.

(a) Model 1.

	FTIR-1[a]	1C3W Hayashi & Ohmine[b]	1C3W QM/MM (model 1)	1C3W empirical eq.[c] (model 1)	2NTU QM/MM (model 1)	2NTU empirical eq.[c] (model 1)
W402…Asp85	2171 (lowest)	2257	2221	2258	2247	2293
W402…Asp212	2636	2618	2663	2564	2646	2548
W401…Asp85	2323	2320	2133 (lowest)	2173 (lowest)	2169 (lowest)	2229 (lowest)
W401…(n.d.)	2690	2721	2703	2727	2704	2727
W406…W401	2599	2601	2515	2454	2514	2463
W406…Asp212	2292	2468	2434	2375	2437	2418
R^2 **to FTIR**		**0.89**	**0.75**	**0.75**	**0.76**	**0.71**

[a] See Ref. (7).

[b] See Ref. (8).

[c] See Ref. (34).

Table 2.

(b) Model 2. The QM/MM results of model 2 on the basis of the 1C3W structure primarily discussed in the present study.

	FTIR-2 [a]	1C3W QM/MM (model 2)	1C3W empirical eq.[b] (model 2)	2NTU QM/MM (model 2)	2NTU empirical eq.[b] (model 2)
W402…Asp85	2171 (lowest)	2078 (lowest)	2201 (lowest)	2120 (lowest)	2240 (lowest)
W402…Asp212	2599	2690	2592	2670	2572
W401…Asp85	2323	2400	2311	2411	2359
W406…(n.d.)	2690	2678	2727	2689	2727
W406…W401	2636	2658	2620	2656	2622
W406…Asp212	2292	2312	2303	2302	2328
R^2 **to FTIR**[c]		0.94[c]	0.99[c]	0.96[c]	0.98[c]

[a] See Ref. (7).

[b] See Ref. (34).

[c] Relative to "FTIR-2."

13

Table 3. H-bond geometries near W402 in the ASR crystal structure (PDB ID code 1XIO at 2.00 Å resolution) and the QM/MM geometry. n.d. = not determined. See Table S1 in the SI for the atomic coordinates of the QM/MM geometries. Distances in Å, angles in °.

	1XIO	**QM/MM**
		Deprotonated Asp75
Donor…acceptor		
W402…Asp75	2.74	2.71
W402…Tyr51	2.92	2.97
Trp76…W402	2.94	2.84
Lys210…W402	3.02	3.00
RMSD[a]	n. d.	0.17
angle(N_{Lys210}…O_{W402}…O_{Asp75})	83	92

[a] Excluding Lys210 due to obvious displacement of the sidechain carbon atoms from the original crystal structure (Figure 2c).

Table 4. O–D stretching frequencies (in cm^{-1}) of W402 in ASR.

| | FTIR[a] | deprotonated Asp75 | |
		QM/MM	Empirical eq.
W402…Asp75	>2500	2376	2392
W402…Tyr51	>2500	2573	2583

[a] See Ref. (11).

Table 5. Contribution of residues to the pK_a shifts of Asp85 in BR and Asp75 in ASR (relative to the bulk solvent) in the presence of the protonated Schiff base (in pK_a units). For clarity, residue pairs that are responsible for differences of <0.7 between pK_a(Asp85) and pK_a(Asp75) are not listed, except for the Glu204/Asp198 pair.

side = sidechain, b.b. = backbone.

BR	pK_a(Asp85) = 1.5			ASR	pK_a(Asp75) = -5.1			difference
(1C3W)	side	b.b.	total	(1XIO)	side	b.b.	total	total
Ile52	-0.1	0.0	-0.1	Trp46	-0.6	-0.3	-0.9	0.8
Ala53	0.0	-0.5	-0.5	Ser47	-2.6	-0.6	-3.2	2.7
Tyr57	-0.5	-0.4	-0.9	Tyr51	0.2	-0.4	-0.2	-0.7
Arg82	-3.9	0.8	-3.1	Arg72	-2.1	0.9	-1.2	-1.9
Glu194	1.2	-0.1	1.1	Ser188	0.0	0.0	0.0	1.1
Glu204	0.0	0.1	0.1	Asp198	0.6	0.0	0.6	-0.5
Asp212	6.3	-0.1	6.2	Pro206			-0.1	6.3
Schiff			-9.3	Schiff			-10.3	1.0

Table 6. Key residues that alter the pK_a difference between Asp85 and Asp212 in the presence of the protonated Schiff base (in pK_a units).

side = side chain, b.b. = backbone, n.d. = not determined.

BR (1C3W)	pK_a(Asp85) = 1.5			pK_a(Asp212) = -2.0		
residue	side	b.b.	total	side	b.b.	total
Met56	-0.4	-0.8	-1.2	-0.1	-0.3	-0.3
Tyr57	-0.5	-0.3	-0.9	-3.2	-0.2	-3.4
Ala81	0.0	0.7	0.8	0.0	0.1	0.1
Arg82	-3.9	0.8	-3.1	-6.4	0.1	-6.3
Asp85	n.d.	n.d.	n.d.	6.4	-0.4	6.0
Trp86	-0.2	-0.6	-0.8	-0.8	-0.3	-1.0
Thr89	-2.0	-0.9	-2.9	0.1	-0.2	-0.1
Tyr185	-0.3	-0.1	-0.4	-3.2	-0.1	-3.3
Glu194	1.2	-0.1	1.2	1.8	-0.1	1.7
Phe208	0.0	0.2	0.2	0.0	1.8	1.8
Asp212	6.3	-0.1	6.2	n.d.	n.d.	n.d.
Schiff	-9.5	0.2	-9.3	-9.3	0.6	-8.7
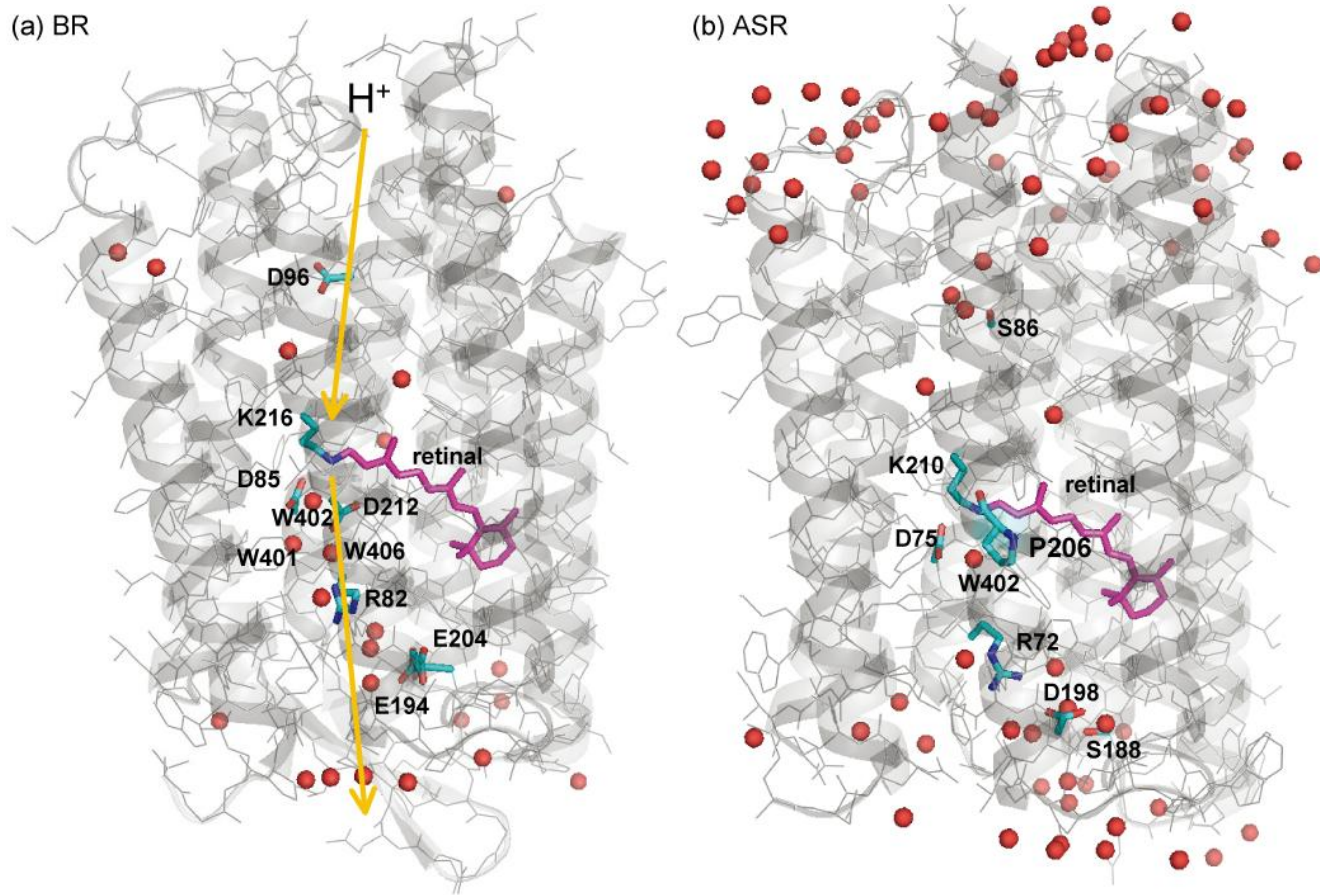
Figure 1.
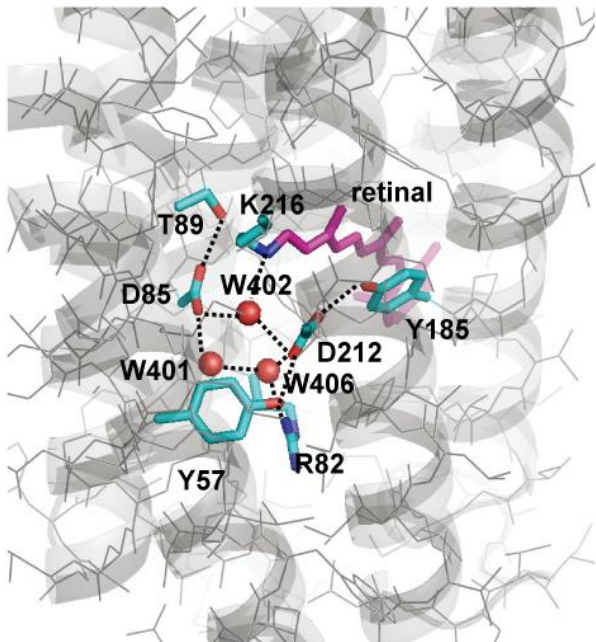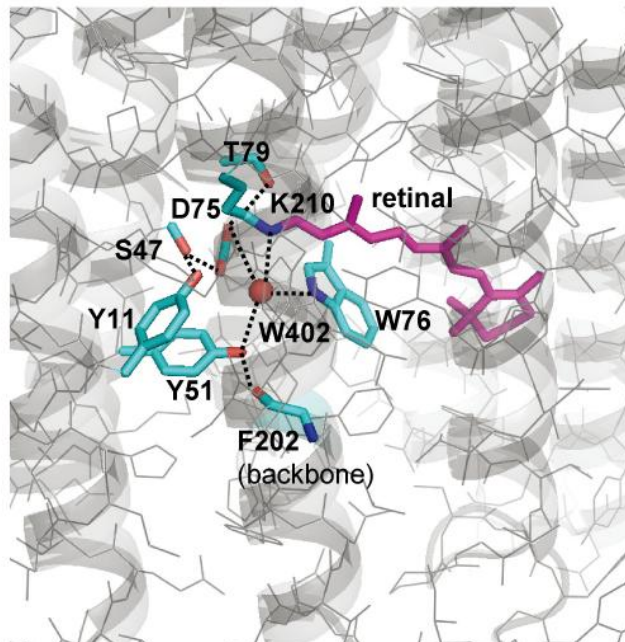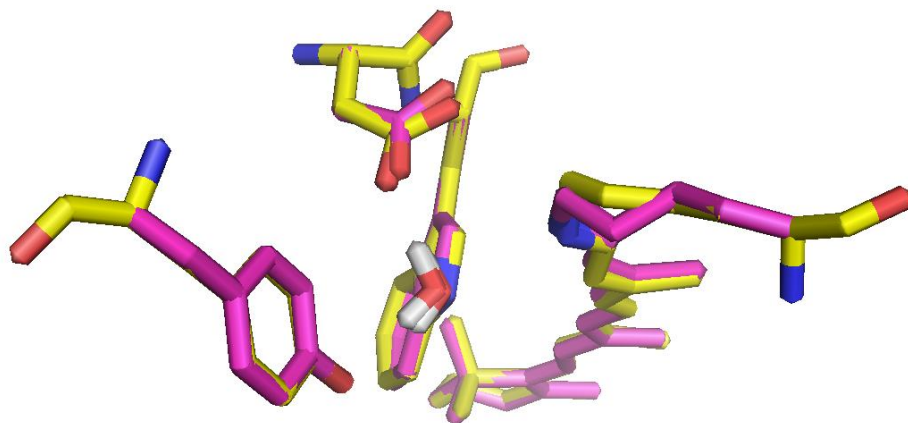
Figure 2 (a, b).

Figure 2 (c).
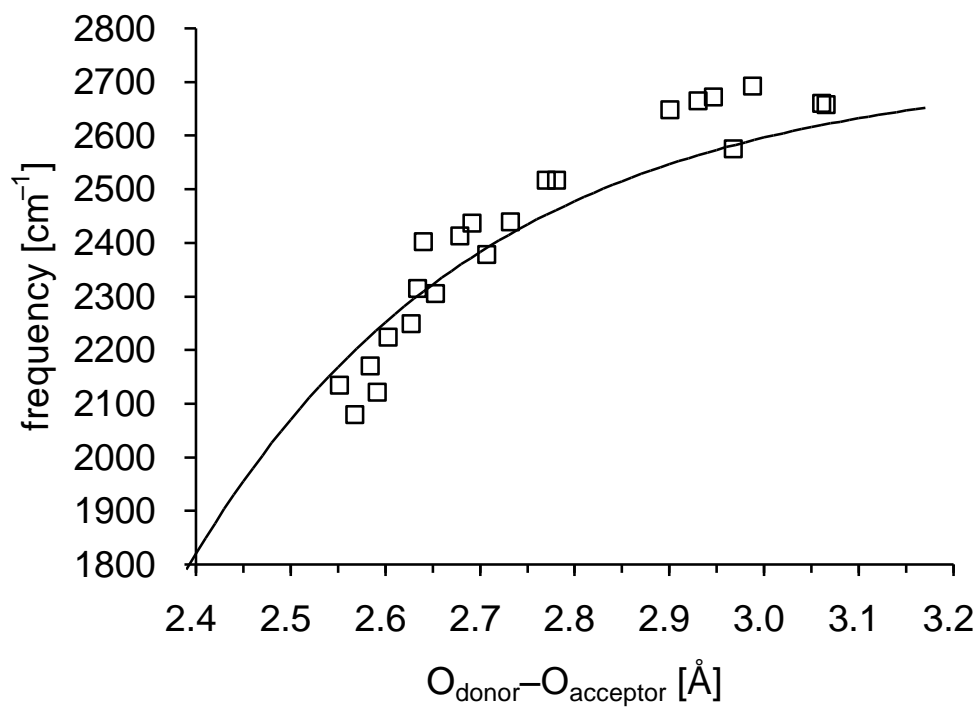
Figure 3.
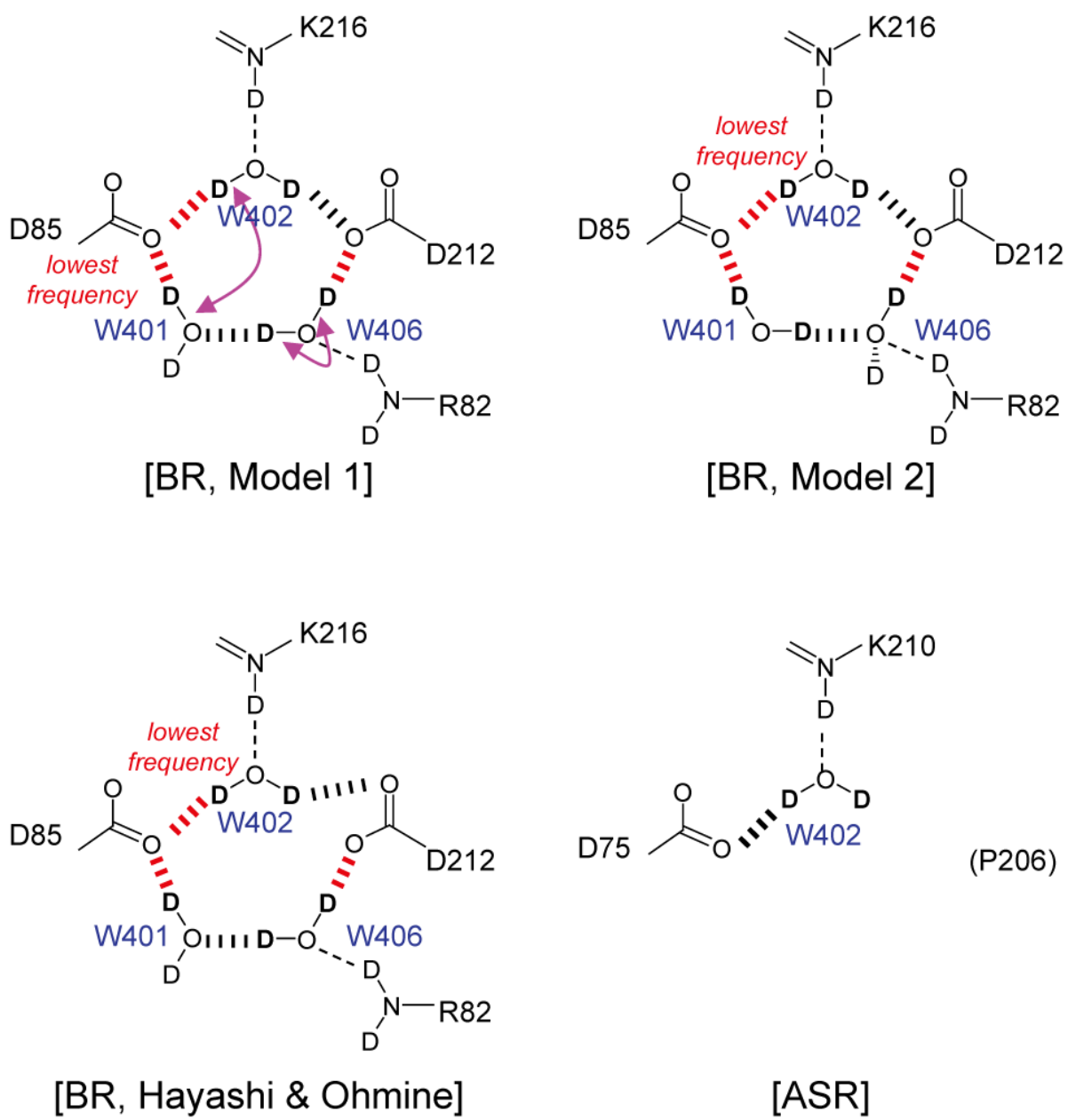
Figure 4.
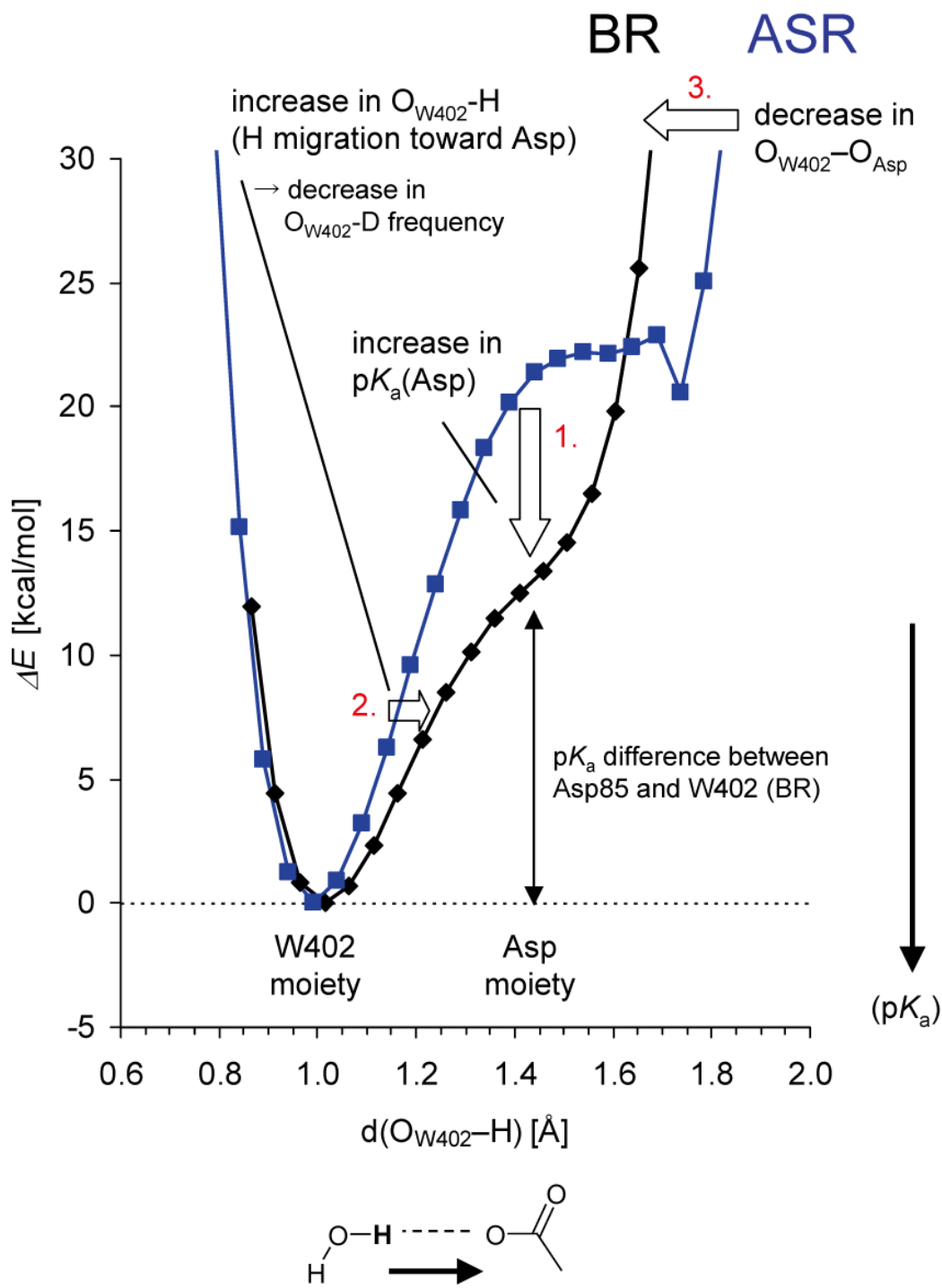
Figure 5.

(a) BR   (b) ASR
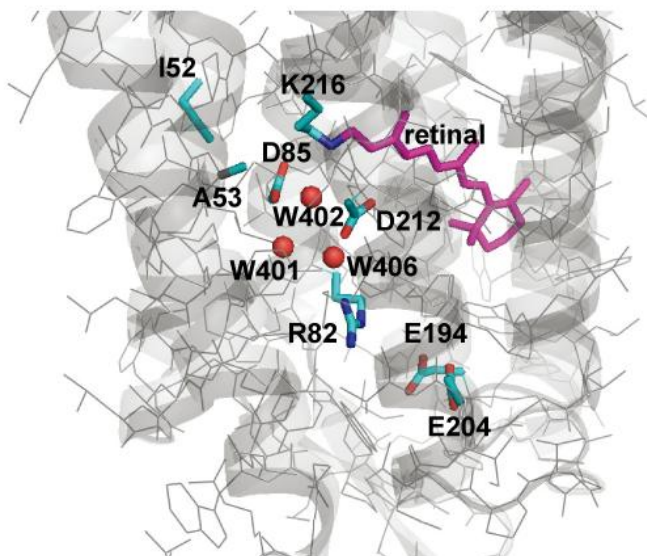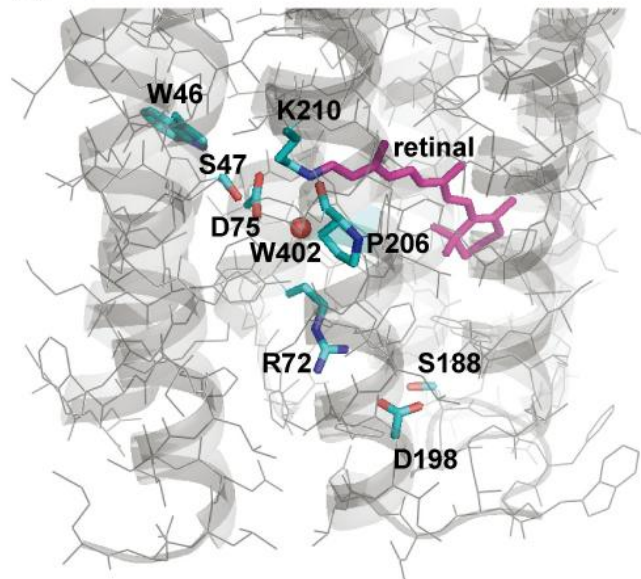
Figure 6.

Factors that differentiate the H-bond strengths of water

near the Schiff bases

in bacteriorhodopsin and *Anabaena* sensory rhodopsin

Keisuke Saito, Hideki Kandori, and Hiroshi Ishikita*

Table S1. Atomic coordinates of the QM/MM optimized geometry for BR [W401, W402, W406, Tyr57,

Arg82, Asp85, Thr89, Tyr185, Asp212, Lys216 (the Shiff base) and the retinal].

(a) 1C3W (model 1)

residue		atom		x	y	z
ARG	A	82	CB	14.733	36.929	-2.302
ARG	A	82	HB1	15.162	37.353	-1.391
ARG	A	82	HB2	14.176	37.735	-2.799
ARG	A	82	CG	15.861	36.483	-3.21
ARG	A	82	HG1	15.528	36.352	-4.243
ARG	A	82	HG2	16.291	35.541	-2.87
ARG	A	82	CD	16.925	37.572	-3.181
ARG	A	82	HD1	17.371	37.628	-2.187
ARG	A	82	HD2	16.494	38.545	-3.42
ARG	A	82	NE	17.958	37.321	-4.161
ARG	A	82	HE	17.955	37.866	-5.04
ARG	A	82	CZ	18.912	36.413	-4.065
ARG	A	82	NH1	19.066	35.659	-2.979
ARG	A	82	HH11	18.435	35.684	-2.155
ARG	A	82	HH12	19.894	35.071	-2.935
ARG	A	82	NH2	19.727	36.23	-5.134
ARG	A	82	HH21	19.679	36.905	-5.893
ARG	A	82	HH22	20.569	35.69	-5.009
ASP	A	85	CB	13.183	33.56	1.776
ASP	A	85	HB1	13.478	34.483	1.278
ASP	A	85	HB2	13.239	32.845	0.967
ASP	A	85	CG	14.378	33.28	2.695
ASP	A	85	OD1	14.364	33.431	3.929
ASP	A	85	OD2	15.428	32.917	2.042
ASP	A	212	CB	20.879	34.919	2.914
ASP	A	212	HB1	20.234	34.146	3.344
ASP	A	212	HB2	21.559	34.43	2.212
ASP	A	212	CG	19.886	35.803	2.158
ASP	A	212	OD1	19.395	36.831	2.662
ASP	A	212	OD2	19.491	35.319	1.033
TYR	A	57	CB	18.451	28.758	-1.114
TYR	A	57	HB1	19.199	28.139	-1.589
TYR	A	57	HB2	18.125	28.236	-0.217
TYR	A	57	CG	19.121	30.08	-0.848
TYR	A	57	CD1	18.793	30.923	0.216
TYR	A	57	HD1	18.074	30.612	0.962
TYR	A	57	CE1	19.357	32.189	0.332
TYR	A	57	HE1	19.07	32.83	1.155
TYR	A	57	CZ	20.257	32.65	-0.64
TYR	A	57	OH	20.72	33.915	-0.634
TYR	A	57	HH	20.274	34.489	0.098
TYR	A	57	CD2	20.101	30.515	-1.752
TYR	A	57	HD2	20.394	29.853	-2.564
TYR	A	57	CE2	20.675	31.778	-1.657
TYR	A	57	HE2	21.412	32.105	-2.382
TYR	A	185	CB	19.172	43.743	2.258
TYR	A	185	HB1	18.377	43.664	1.513

TYR	A	185 HB2	18.767	44.326	3.088
TYR	A	185 CG	19.52	42.353	2.737
TYR	A	185 CD1	20.268	42.19	3.9
TYR	A	185 HD1	20.633	43.08	4.378
TYR	A	185 CE1	20.548	40.951	4.451
TYR	A	185 HE1	21.122	40.855	5.366
TYR	A	185 CZ	20.084	39.807	3.801
TYR	A	185 OH	20.332	38.611	4.382
TYR	A	185 HH	20.005	37.882	3.796
TYR	A	185 CD2	19.06	41.197	2.104
TYR	A	185 HD2	18.443	41.276	1.216
TYR	A	185 CE2	19.358	39.933	2.61
TYR	A	185 HE2	19.001	39.039	2.114
THR	A	89 CB	13.525	34.153	7.186
THR	A	89 HB	14.346	34.097	7.913
THR	A	89 OG1	13.966	35.005	6.142
THR	A	89 HG1	13.87	34.535	5.292
THR	A	89 CG2	13.189	32.74	6.718
THR	A	89 HG21	12.422	32.755	5.943
THR	A	89 HG22	12.81	32.133	7.545
THR	A	89 HG23	14.065	32.249	6.293
LYS	A	216 CB	19.893	32.654	8.085
LYS	A	216 HB1	19.393	31.733	8.411
LYS	A	216 HB2	20.648	32.351	7.352
LYS	A	216 CG	18.877	33.605	7.446
LYS	A	216 HG1	19.386	34.456	6.987
LYS	A	216 HG2	18.239	34.032	8.227
LYS	A	216 CD	17.978	32.944	6.407
LYS	A	216 HD1	17.583	31.994	6.785
LYS	A	216 HD2	18.528	32.712	5.492
LYS	A	216 CE	16.805	33.859	6.066
LYS	A	216 HE1	16.292	34.19	6.969
LYS	A	216 HE2	16.06	33.387	5.427
LYS	A	216 NZ	17.246	35.053	5.368
LYS	A	216 HZ1	17.404	34.926	4.357
HOH		402 O	17.687	33.915	2.868
HOH		402 H1	17.98	34.384	2.073
HOH		402 H2	16.81	33.489	2.627
HOH		401 O	16.112	33.207	-0.4
HOH		401 H1	15.746	33.082	0.528
HOH		401 H2	16.816	32.55	-0.483
HOH		406 O	17.486	35.589	-0.744
HOH		406 H1	16.939	34.786	-0.588
HOH		406 H2	18.131	35.647	-0.008
RTAL		301 C1	14.874	45.074	0.303
RTAL		301 C2	14.774	45.988	-0.938
RTAL		301 H21	14.308	45.416	-1.741
RTAL		301 H22	15.791	46.237	-1.265
RTAL		301 C3	14.02	47.282	-0.724
RTAL		301 H31	12.981	47.066	-0.471
RTAL		301 H32	13.995	47.853	-1.658
RTAL		301 C4	14.724	48.066	0.379
RTAL		301 H41	14.15	48.946	0.693
RTAL		301 H42	15.652	48.492	-0.025
RTAL		301 C5	15.062	47.233	1.599

RTAL	301 C6	15.157	45.873	1.58
RTAL	301 C7	15.498	45.176	2.812
RTAL	301 H71	15.837	45.798	3.63
RTAL	301 C8	15.497	43.842	3.061
RTAL	301 H81	15.129	43.141	2.326
RTAL	301 C9	16.055	43.227	4.233
RTAL	301 C10	16.193	41.863	4.193
RTAL	301 H101	15.834	41.354	3.301
RTAL	301 C11	16.824	41.027	5.149
RTAL	301 H111	17.126	41.424	6.114
RTAL	301 C12	17.031	39.71	4.84
RTAL	301 H121	16.723	39.382	3.853
RTAL	301 C13	17.49	38.689	5.711
RTAL	301 C14	17.499	37.406	5.192
RTAL	301 H141	17.461	37.302	4.12
RTAL	301 C15	17.349	36.236	5.932
RTAL	301 H15	17.194	36.268	7.005
RTAL	301 C16	13.524	44.339	0.492
RTAL	301 H161	13.238	43.888	-0.457
RTAL	301 H162	12.74	45.034	0.806
RTAL	301 H163	13.563	43.545	1.238
RTAL	301 C17	16.018	44.093	-0.04
RTAL	301 H171	16.959	44.637	-0.16
RTAL	301 H172	15.8	43.609	-0.995
RTAL	301 H173	16.179	43.311	0.697
RTAL	301 C18	15.215	48.039	2.857
RTAL	301 H181	14.243	48.181	3.345
RTAL	301 H182	15.611	49.025	2.625
RTAL	301 H183	15.866	47.594	3.603
RTAL	301 C19	16.581	44.061	5.361
RTAL	301 H191	15.867	44.825	5.666
RTAL	301 H192	17.494	44.579	5.059
RTAL	301 H193	16.808	43.445	6.225
RTAL	301 C20	17.929	38.991	7.105
RTAL	301 H201	17.237	39.646	7.628
RTAL	301 H202	18.89	39.516	7.053
RTAL	301 H203	18.086	38.088	7.695

(b) 1C3W (model 2)

residue		atom		x	y	z
ARG	A	82	CB	14.716	36.94	-2.32
ARG	A	82	HB1	15.108	37.429	-1.422
ARG	A	82	HB2	14.149	37.713	-2.855
ARG	A	82	CG	15.871	36.492	-3.191
ARG	A	82	HG1	15.553	36.313	-4.222
ARG	A	82	HG2	16.312	35.568	-2.814
ARG	A	82	CD	16.91	37.607	-3.198
ARG	A	82	HD1	17.336	37.739	-2.201
ARG	A	82	HD2	16.466	38.557	-3.494
ARG	A	82	NE	17.976	37.324	-4.132
ARG	A	82	HE	18.016	37.848	-5.026
ARG	A	82	CZ	18.914	36.414	-3.944
ARG	A	82	NH1	19.004	35.725	-2.804
ARG	A	82	HH11	18.337	35.829	-2.036
ARG	A	82	HH12	19.779	35.083	-2.677
ARG	A	82	NH2	19.781	36.164	-4.949
ARG	A	82	HH21	19.784	36.767	-5.764
ARG	A	82	HH22	20.589	35.589	-4.743
ASP	A	85	CB	13.185	33.544	1.792
ASP	A	85	HB1	13.47	34.438	1.24
ASP	A	85	HB2	13.249	32.788	1.024
ASP	A	85	CG	14.391	33.314	2.718
ASP	A	85	OD1	14.376	33.501	3.951
ASP	A	85	OD2	15.441	32.952	2.073
ASP	A	212	CB	20.87	34.929	2.914
ASP	A	212	HB1	20.226	34.154	3.345
ASP	A	212	HB2	21.545	34.442	2.208
ASP	A	212	CG	19.871	35.814	2.165
ASP	A	212	OD1	19.349	36.818	2.688
ASP	A	212	OD2	19.496	35.354	1.023
TYR	A	57	CB	18.454	28.766	-1.12
TYR	A	57	HB1	19.207	28.151	-1.595
TYR	A	57	HB2	18.132	28.244	-0.22
TYR	A	57	CG	19.11	30.096	-0.859
TYR	A	57	CD1	18.677	30.993	0.119
TYR	A	57	HD1	17.859	30.744	0.78
TYR	A	57	CE1	19.239	32.257	0.226
TYR	A	57	HE1	18.867	32.943	0.973
TYR	A	57	CZ	20.235	32.663	-0.668
TYR	A	57	OH	20.71	33.934	-0.668
TYR	A	57	HH	20.283	34.5	0.065
TYR	A	57	CD2	20.161	30.49	-1.699
TYR	A	57	HD2	20.519	29.792	-2.453
TYR	A	57	CE2	20.732	31.756	-1.612
TYR	A	57	HE2	21.529	32.055	-2.286
TYR	A	185	CB	19.175	43.742	2.26
TYR	A	185	HB1	18.377	43.663	1.516
TYR	A	185	HB2	18.772	44.322	3.091
TYR	A	185	CG	19.524	42.352	2.737

5

TYR	A	185 CD1	20.279	42.189	3.897
TYR	A	185 HD1	20.647	43.078	4.373
TYR	A	185 CE1	20.557	40.95	4.449
TYR	A	185 HE1	21.134	40.854	5.363
TYR	A	185 CZ	20.086	39.806	3.804
TYR	A	185 OH	20.332	38.61	4.388
TYR	A	185 HH	19.984	37.882	3.815
TYR	A	185 CD2	19.058	41.196	2.109
TYR	A	185 HD2	18.436	41.276	1.223
TYR	A	185 CE2	19.355	39.932	2.615
TYR	A	185 HE2	18.995	39.038	2.124
THR	A	89 CB	13.524	34.158	7.187
THR	A	89 HB	14.34	34.092	7.921
THR	A	89 OG1	13.971	35.019	6.155
THR	A	89 HG1	13.886	34.553	5.299
THR	A	89 CG2	13.187	32.749	6.707
THR	A	89 HG21	12.427	32.769	5.926
THR	A	89 HG22	12.801	32.139	7.529
THR	A	89 HG23	14.065	32.257	6.286
LYS	A	216 CB	19.897	32.655	8.084
LYS	A	216 HB1	19.398	31.733	8.408
LYS	A	216 HB2	20.653	32.354	7.352
LYS	A	216 CG	18.881	33.604	7.445
LYS	A	216 HG1	19.39	34.454	6.983
LYS	A	216 HG2	18.245	34.034	8.227
LYS	A	216 CD	17.977	32.942	6.411
LYS	A	216 HD1	17.587	31.99	6.789
LYS	A	216 HD2	18.52	32.713	5.49
LYS	A	216 CE	16.798	33.854	6.081
LYS	A	216 HE1	16.29	34.183	6.986
LYS	A	216 HE2	16.051	33.384	5.442
LYS	A	216 NZ	17.232	35.05	5.383
LYS	A	216 HZ1	17.388	34.918	4.369
HOH		402 O	17.669	33.922	2.906
HOH		402 H1	17.968	34.368	2.101
HOH		402 H2	16.789	33.486	2.653
HOH		401 O	15.754	33.013	-0.549
HOH		401 H1	15.588	32.944	0.422
HOH		401 H2	16.345	33.777	-0.634
HOH		406 O	17.34	35.631	-0.467
HOH		406 H1	16.641	36.19	-0.093
HOH		406 H2	18.102	35.669	0.17
RTAL		301 C1	14.867	45.06	0.321
RTAL		301 C2	14.764	45.965	-0.927
RTAL		301 H21	14.293	45.386	-1.723
RTAL		301 H22	15.779	46.209	-1.26
RTAL		301 C3	14.014	47.264	-0.721
RTAL		301 H31	12.974	47.055	-0.467
RTAL		301 H32	13.992	47.829	-1.659
RTAL		301 C4	14.719	48.053	0.377
RTAL		301 H41	14.147	48.937	0.684
RTAL		301 H42	15.648	48.473	-0.03
RTAL		301 C5	15.054	47.227	1.603
RTAL		301 C6	15.151	45.867	1.592
RTAL		301 C7	15.499	45.176	2.826

RTAL	301 H71	15.836	45.803	3.642
RTAL	301 C8	15.51	43.843	3.078
RTAL	301 H81	15.142	43.138	2.346
RTAL	301 C9	16.079	43.231	4.248
RTAL	301 C10	16.214	41.868	4.212
RTAL	301 H101	15.845	41.358	3.324
RTAL	301 C11	16.844	41.028	5.167
RTAL	301 H111	17.152	41.421	6.131
RTAL	301 C12	17.039	39.709	4.859
RTAL	301 H121	16.722	39.383	3.874
RTAL	301 C13	17.491	38.683	5.729
RTAL	301 C14	17.487	37.402	5.212
RTAL	301 H141	17.442	37.298	4.14
RTAL	301 C15	17.337	36.229	5.949
RTAL	301 H15	17.183	36.259	7.022
RTAL	301 C16	13.52	44.326	0.519
RTAL	301 H161	13.243	43.838	-0.415
RTAL	301 H162	12.73	45.028	0.802
RTAL	301 H163	13.554	43.56	1.294
RTAL	301 C17	16.014	44.08	-0.015
RTAL	301 H171	16.956	44.626	-0.125
RTAL	301 H172	15.806	43.599	-0.974
RTAL	301 H173	16.169	43.295	0.722
RTAL	301 C18	15.209	48.042	2.857
RTAL	301 H181	14.24	48.173	3.353
RTAL	301 H182	15.589	49.031	2.617
RTAL	301 H183	15.872	47.608	3.599
RTAL	301 C19	16.609	44.069	5.37
RTAL	301 H191	15.845	44.736	5.772
RTAL	301 H192	17.434	44.699	5.028
RTAL	301 H193	16.971	43.443	6.181
RTAL	301 C20	17.934	38.98	7.123
RTAL	301 H201	17.233	39.618	7.657
RTAL	301 H202	18.885	39.523	7.072
RTAL	301 H203	18.109	38.074	7.702

(c) 2NTU (model 1)

residue		atom	x	y	z
ARG	A	82 CB	14.748	37.211	-2.273
ARG	A	82 HB1	15.184	37.638	-1.365
ARG	A	82 HB2	14.193	38.019	-2.77
ARG	A	82 CG	15.87	36.75	-3.19
ARG	A	82 HG1	15.52	36.594	-4.217
ARG	A	82 HG2	16.306	35.812	-2.842
ARG	A	82 CD	16.932	37.845	-3.208
ARG	A	82 HD1	17.39	37.935	-2.221
ARG	A	82 HD2	16.491	38.808	-3.469
ARG	A	82 NE	17.957	37.582	-4.198
ARG	A	82 HE	17.942	38.111	-5.083
ARG	A	82 CZ	18.929	36.69	-4.086
ARG	A	82 NH1	19.096	35.953	-2.991
ARG	A	82 HH11	18.491	35.985	-2.145
ARG	A	82 HH12	19.937	35.38	-2.952
ARG	A	82 NH2	19.749	36.504	-5.151
ARG	A	82 HH21	19.695	37.164	-5.922
ARG	A	82 HH22	20.597	35.974	-5.019
ASP	A	85 CB	13.226	33.832	1.815
ASP	A	85 HB1	13.516	34.753	1.309
ASP	A	85 HB2	13.259	33.102	1.014
ASP	A	85 CG	14.429	33.547	2.735
ASP	A	85 OD1	14.412	33.679	3.974
ASP	A	85 OD2	15.479	33.198	2.073
ASP	A	212 CB	20.954	35.152	3.094
ASP	A	212 HB1	20.298	34.39	3.527
ASP	A	212 HB2	21.642	34.642	2.413
ASP	A	212 CG	19.991	36.029	2.285
ASP	A	212 OD1	19.561	37.115	2.716
ASP	A	212 OD2	19.572	35.479	1.198
TYR	A	57 CB	18.602	28.971	-1.201
TYR	A	57 HB1	19.338	28.349	-1.706
TYR	A	57 HB2	18.284	28.432	-0.306
TYR	A	57 CG	19.272	30.289	-0.895
TYR	A	57 CD1	18.921	31.103	0.187
TYR	A	57 HD1	18.197	30.771	0.917
TYR	A	57 CE1	19.47	32.371	0.348
TYR	A	57 HE1	19.164	32.989	1.183
TYR	A	57 CZ	20.388	32.863	-0.59
TYR	A	57 OH	20.847	34.13	-0.538
TYR	A	57 HH	20.397	34.671	0.202
TYR	A	57 CD2	20.265	30.756	-1.766
TYR	A	57 HD2	20.581	30.12	-2.59
TYR	A	57 CE2	20.831	32.019	-1.621
TYR	A	57 HE2	21.583	32.368	-2.322
TYR	A	185 CB	19.289	44.049	2.317
TYR	A	185 HB1	18.483	43.962	1.584
TYR	A	185 HB2	18.897	44.633	3.152
TYR	A	185 CG	19.643	42.663	2.815
TYR	A	185 CD1	20.383	42.505	3.987
TYR	A	185 HD1	20.742	43.393	4.48
TYR	A	185 CE1	20.658	41.263	4.539

8

TYR	A	185 HE1	21.228	41.169	5.459
TYR	A	185 CZ	20.197	40.115	3.892
TYR	A	185 OH	20.451	38.914	4.468
TYR	A	185 HH	20.14	38.186	3.873
TYR	A	185 CD2	19.176	41.503	2.192
TYR	A	185 HD2	18.552	41.577	1.308
TYR	A	185 CE2	19.467	40.239	2.703
TYR	A	185 HE2	19.106	39.345	2.21
THR	A	89 CB	13.567	34.365	7.361
THR	A	89 HB	14.402	34.288	8.071
THR	A	89 OG1	13.997	35.215	6.309
THR	A	89 HG1	13.927	34.738	5.46
THR	A	89 CG2	13.208	32.958	6.882
THR	A	89 HG21	12.446	32.984	6.101
THR	A	89 HG22	12.815	32.348	7.702
THR	A	89 HG23	14.083	32.459	6.463
LYS	A	216 CB	20.002	32.975	8.395
LYS	A	216 HB1	19.514	32.047	8.714
LYS	A	216 HB2	20.757	32.678	7.659
LYS	A	216 CG	18.983	33.908	7.732
LYS	A	216 HG1	19.487	34.774	7.294
LYS	A	216 HG2	18.312	34.312	8.496
LYS	A	216 CD	18.139	33.228	6.655
LYS	A	216 HD1	17.749	32.269	7.018
LYS	A	216 HD2	18.739	33.004	5.769
LYS	A	216 CE	16.955	34.104	6.244
LYS	A	216 HE1	16.39	34.434	7.117
LYS	A	216 HE2	16.252	33.59	5.589
LYS	A	216 NZ	17.378	35.296	5.529
LYS	A	216 HZ1	17.515	35.161	4.516
HOH		402 O	17.751	34.13	3.01
HOH		402 H1	18.114	34.562	2.222
HOH		402 H2	16.872	33.737	2.733
HOH		401 O	16.221	33.469	-0.389
HOH		401 H1	15.83	33.367	0.53
HOH		401 H2	16.916	32.8	-0.442
HOH		406 O	17.631	35.848	-0.691
HOH		406 H1	18.266	35.884	0.056
HOH		406 H2	17.078	35.046	-0.553
RTAL		301 C1	14.962	45.339	0.341
RTAL		301 C2	14.828	46.27	-0.888
RTAL		301 H21	14.365	45.702	-1.699
RTAL		301 H22	15.833	46.545	-1.23
RTAL		301 C3	14.054	47.547	-0.624
RTAL		301 H31	13.031	47.307	-0.328
RTAL		301 H32	13.982	48.138	-1.544
RTAL		301 C4	14.779	48.323	0.469
RTAL		301 H41	14.218	49.198	0.808
RTAL		301 H42	15.703	48.738	0.041
RTAL		301 C5	15.132	47.485	1.676
RTAL		301 C6	15.24	46.125	1.634
RTAL		301 C7	15.573	45.425	2.863
RTAL		301 H71	15.864	46.055	3.692
RTAL		301 C8	15.607	44.088	3.112
RTAL		301 H81	15.305	43.379	2.354

RTAL	301	C9	16.111	43.48	4.312
RTAL	301	C10	16.282	42.117	4.27
RTAL	301	H101	15.987	41.611	3.354
RTAL	301	C11	16.872	41.286	5.252
RTAL	301	H111	17.139	41.693	6.223
RTAL	301	C12	17.095	39.963	4.96
RTAL	301	H121	16.82	39.63	3.965
RTAL	301	C13	17.542	38.952	5.844
RTAL	301	C14	17.575	37.66	5.332
RTAL	301	H141	17.537	37.551	4.258
RTAL	301	C15	17.453	36.493	6.078
RTAL	301	H15	17.31	36.53	7.154
RTAL	301	C16	13.633	44.566	0.523
RTAL	301	H161	13.393	44.037	-0.401
RTAL	301	H162	12.818	45.256	0.759
RTAL	301	H163	13.668	43.831	1.328
RTAL	301	C17	16.125	44.388	-0.02
RTAL	301	H171	17.053	44.954	-0.14
RTAL	301	H172	15.913	43.905	-0.978
RTAL	301	H173	16.307	43.605	0.714
RTAL	301	C18	15.268	48.288	2.938
RTAL	301	H181	14.269	48.449	3.36
RTAL	301	H182	15.694	49.264	2.711
RTAL	301	H183	15.882	47.834	3.712
RTAL	301	C19	16.543	44.31	5.487
RTAL	301	H191	15.904	45.182	5.63
RTAL	301	H192	17.564	44.675	5.34
RTAL	301	H193	16.519	43.724	6.405
RTAL	301	C20	17.961	39.272	7.244
RTAL	301	H201	17.301	39.991	7.724
RTAL	301	H202	18.957	39.729	7.203
RTAL	301	H203	18.038	38.384	7.871

(d) 2NTU (model 2)

residue		atom		x	y	z
ARG	A	82	CB	14.733	37.219	-2.288
ARG	A	82	HB1	15.136	37.7	-1.39
ARG	A	82	HB2	14.167	37.999	-2.815
ARG	A	82	CG	15.88	36.76	-3.176
ARG	A	82	HG1	15.542	36.555	-4.197
ARG	A	82	HG2	16.334	35.844	-2.792
ARG	A	82	CD	16.912	37.885	-3.238
ARG	A	82	HD1	17.352	38.059	-2.251
ARG	A	82	HD2	16.451	38.819	-3.559
ARG	A	82	NE	17.97	37.594	-4.185
ARG	A	82	HE	17.988	38.101	-5.086
ARG	A	82	CZ	18.936	36.709	-3.998
ARG	A	82	NH1	19.056	36.026	-2.857
ARG	A	82	HH11	18.425	36.134	-2.058
ARG	A	82	HH12	19.863	35.418	-2.749
ARG	A	82	NH2	19.802	36.472	-5.008
ARG	A	82	HH21	19.782	37.064	-5.831
ARG	A	82	HH22	20.616	35.904	-4.814
ASP	A	85	CB	13.228	33.821	1.827
ASP	A	85	HB1	13.515	34.727	1.296
ASP	A	85	HB2	13.265	33.073	1.043
ASP	A	85	CG	14.433	33.557	2.758
ASP	A	85	OD1	14.405	33.7	3.999
ASP	A	85	OD2	15.486	33.219	2.107
ASP	A	212	CB	20.947	35.16	3.094
ASP	A	212	HB1	20.291	34.398	3.528
ASP	A	212	HB2	21.63	34.651	2.409
ASP	A	212	CG	19.979	36.039	2.292
ASP	A	212	OD1	19.525	37.111	2.737
ASP	A	212	OD2	19.575	35.507	1.189
TYR	A	57	CB	18.607	28.985	-1.208
TYR	A	57	HB1	19.348	28.367	-1.711
TYR	A	57	HB2	18.295	28.45	-0.308
TYR	A	57	CG	19.259	30.314	-0.915
TYR	A	57	CD1	18.778	31.201	0.052
TYR	A	57	HD1	17.928	30.947	0.667
TYR	A	57	CE1	19.331	32.463	0.209
TYR	A	57	HE1	18.925	33.138	0.948
TYR	A	57	CZ	20.374	32.88	-0.623
TYR	A	57	OH	20.853	34.15	-0.573
TYR	A	57	HH	20.416	34.686	0.165
TYR	A	57	CD2	20.35	30.722	-1.696
TYR	A	57	HD2	20.748	30.036	-2.44
TYR	A	57	CE2	20.915	31.989	-1.558
TYR	A	57	HE2	21.745	32.298	-2.187
TYR	A	185	CB	19.29	44.049	2.318
TYR	A	185	HB1	18.482	43.962	1.586
TYR	A	185	HB2	18.899	44.632	3.153
TYR	A	185	CG	19.644	42.664	2.814
TYR	A	185	CD1	20.391	42.508	3.981
TYR	A	185	HD1	20.755	43.397	4.468
TYR	A	185	CE1	20.665	41.267	4.537

TYR	A	185 HE1	21.239	41.176	5.454
TYR	A	185 CZ	20.196	40.118	3.896
TYR	A	185 OH	20.451	38.918	4.475
TYR	A	185 HH	20.125	38.19	3.89
TYR	A	185 CD2	19.17	41.504	2.197
TYR	A	185 HD2	18.54	41.578	1.317
TYR	A	185 CE2	19.461	40.24	2.711
TYR	A	185 HE2	19.097	39.346	2.223
THR	A	89 CB	13.568	34.362	7.362
THR	A	89 HB	14.401	34.278	8.075
THR	A	89 OG1	14.002	35.214	6.313
THR	A	89 HG1	13.942	34.736	5.462
THR	A	89 CG2	13.205	32.957	6.879
THR	A	89 HG21	12.446	32.987	6.094
THR	A	89 HG22	12.806	32.348	7.697
THR	A	89 HG23	14.079	32.453	6.462
LYS	A	216 CB	20	32.974	8.398
LYS	A	216 HB1	19.506	32.05	8.721
LYS	A	216 HB2	20.754	32.669	7.663
LYS	A	216 CG	18.986	33.908	7.73
LYS	A	216 HG1	19.495	34.768	7.285
LYS	A	216 HG2	18.32	34.321	8.493
LYS	A	216 CD	18.134	33.224	6.661
LYS	A	216 HD1	17.75	32.265	7.028
LYS	A	216 HD2	18.726	33	5.77
LYS	A	216 CE	16.943	34.096	6.26
LYS	A	216 HE1	16.383	34.423	7.138
LYS	A	216 HE2	16.238	33.582	5.607
LYS	A	216 NZ	17.357	35.292	5.546
LYS	A	216 HZ1	17.484	35.157	4.529
HOH		402 O	17.709	34.173	3.04
HOH		402 H1	18.096	34.556	2.24
HOH		402 H2	16.838	33.75	2.75
HOH		401 O	15.873	33.336	-0.542
HOH		401 H1	15.675	33.256	0.422
HOH		401 H2	16.494	34.08	-0.599
HOH		406 O	17.525	35.918	-0.446
HOH		406 H1	18.262	35.901	0.223
HOH		406 H2	16.826	36.47	-0.065
RTAL		301 C1	14.962	45.329	0.352
RTAL		301 C2	14.819	46.256	-0.88
RTAL		301 H21	14.352	45.683	-1.686
RTAL		301 H22	15.823	46.528	-1.23
RTAL		301 C3	14.048	47.534	-0.619
RTAL		301 H31	13.026	47.298	-0.32
RTAL		301 H32	13.976	48.124	-1.54
RTAL		301 C4	14.776	48.314	0.471
RTAL		301 H41	14.216	49.189	0.808
RTAL		301 H42	15.698	48.727	0.039
RTAL		301 C5	15.132	47.48	1.681
RTAL		301 C6	15.245	46.119	1.642
RTAL		301 C7	15.591	45.421	2.87
RTAL		301 H71	15.887	46.053	3.696
RTAL		301 C8	15.632	44.085	3.122
RTAL		301 H81	15.322	43.372	2.37

RTAL	301 C9	16.15	43.483	4.32
RTAL	301 C10	16.307	42.118	4.291
RTAL	301 H101	15.994	41.608	3.382
RTAL	301 C11	16.896	41.283	5.271
RTAL	301 H111	17.174	41.686	6.24
RTAL	301 C12	17.102	39.958	4.98
RTAL	301 H121	16.814	39.625	3.988
RTAL	301 C13	17.545	38.943	5.863
RTAL	301 C14	17.562	37.653	5.354
RTAL	301 H141	17.511	37.543	4.281
RTAL	301 C15	17.443	36.483	6.1
RTAL	301 H15	17.31	36.518	7.177
RTAL	301 C16	13.635	44.555	0.542
RTAL	301 H161	13.4	44.005	-0.371
RTAL	301 H162	12.815	45.246	0.761
RTAL	301 H163	13.669	43.837	1.363
RTAL	301 C17	16.124	44.379	-0.015
RTAL	301 H171	17.053	44.946	-0.13
RTAL	301 H172	15.915	43.905	-0.978
RTAL	301 H173	16.305	43.59	0.712
RTAL	301 C18	15.266	48.29	2.939
RTAL	301 H181	14.267	48.447	3.36
RTAL	301 H182	15.686	49.268	2.71
RTAL	301 H183	15.881	47.841	3.715
RTAL	301 C19	16.601	44.326	5.477
RTAL	301 H191	15.863	45.087	5.732
RTAL	301 H192	17.529	44.85	5.229
RTAL	301 H193	16.775	43.719	6.363
RTAL	301 C20	17.974	39.261	7.261
RTAL	301 H201	17.301	39.959	7.756
RTAL	301 H202	18.957	39.744	7.213
RTAL	301 H203	18.08	38.369	7.878

Table S2. Atomic coordinates of the QM/MM optimized geometry for ASR [W402, Tyr11, Tyr51, Asp75, Trp76, Thr79, Ser47, the backbone of Phe202, Lys210 (the Schiff base) and the retinal].

1XIO (deprotonated Asp75)

residue		atom	x	y	z
TYR	A	11 CB	28.683	32.043	23.475
TYR	A	11 HB1	29.208	32.866	23.952
TYR	A	11 HB2	28.175	32.457	22.597
TYR	A	11 CG	29.664	30.969	23.082
TYR	A	11 CD1	29.352	30.066	22.066
TYR	A	11 HD1	28.405	30.148	21.539
TYR	A	11 CE1	30.236	29.054	21.722
TYR	A	11 HE1	29.956	28.336	20.969
TYR	A	11 CZ	31.467	28.925	22.373
TYR	A	11 OH	32.302	27.928	21.976
TYR	A	11 HH	33.133	27.936	22.512
TYR	A	11 CD2	30.878	30.802	23.759
TYR	A	11 HD2	31.123	31.475	24.574
TYR	A	11 CE2	31.782	29.801	23.416
TYR	A	11 HE2	32.735	29.716	23.927
TYR	A	51 CB	33.276	33.098	25.01
TYR	A	51 HB1	32.369	33.707	25.086
TYR	A	51 HB2	33.13	32.21	25.638
TYR	A	51 CG	33.493	32.727	23.547
TYR	A	51 CD1	34.614	32.028	23.071
TYR	A	51 HD1	35.404	31.705	23.737
TYR	A	51 CE1	34.764	31.711	21.727
TYR	A	51 HE1	35.648	31.178	21.404
TYR	A	51 CZ	33.767	32.05	20.812
TYR	A	51 OH	33.953	31.654	19.506
TYR	A	51 HH	33.22	31.982	18.944
TYR	A	51 CD2	32.518	33.062	22.602
TYR	A	51 HD2	31.614	33.553	22.948
TYR	A	51 CE2	32.632	32.735	21.25
TYR	A	51 HE2	31.849	32.996	20.548
ASP	A	75 CB	38.833	29.43	22.443
ASP	A	75 HB1	38.814	30.216	21.689
ASP	A	75 HB2	38.631	29.939	23.383
ASP	A	75 CG	37.618	28.525	22.171
ASP	A	75 OD1	37.662	27.273	22.244
ASP	A	75 OD2	36.54	29.182	21.953
TRP	A	76 CB	40.705	27.733	17.857
TRP	A	76 HB1	40.923	26.964	17.11
TRP	A	76 HB2	41.52	28.465	17.807
TRP	A	76 CG	39.4	28.405	17.529
TRP	A	76 CD1	38.175	28.269	18.132
TRP	A	76 HD1	37.904	27.718	19.022
TRP	A	76 NE1	37.205	28.987	17.456
TRP	A	76 HE1	36.34	29.236	17.936
TRP	A	76 CE2	37.81	29.657	16.41
TRP	A	76 CD2	39.193	29.315	16.423
TRP	A	76 CE3	40.044	29.927	15.482

TRP	A	76 HE3	41.111	29.725	15.488
TRP	A	76 CZ3	39.514	30.836	14.569
TRP	A	76 HZ3	40.169	31.345	13.87
TRP	A	76 CZ2	37.267	30.535	15.463
TRP	A	76 HZ2	36.204	30.759	15.452
TRP	A	76 CH2	38.136	31.134	14.551
TRP	A	76 HH2	37.755	31.856	13.836
THR	A	79 CB	38.473	23.841	21.882
THR	A	79 HB	37.622	23.177	21.659
THR	A	79 OG1	38.448	24.87	20.899
THR	A	79 HG1	38.395	25.736	21.353
THR	A	79 CG2	38.308	24.372	23.299
THR	A	79 HG21	39.101	25.078	23.545
THR	A	79 HG22	38.334	23.561	24.035
THR	A	79 HG23	37.359	24.898	23.411
SER	A	47 CB	35.096	27.085	24.338
SER	A	47 HB1	34.234	26.62	24.822
SER	A	47 HB2	35.756	26.296	23.961
SER	A	47 OG	34.614	27.899	23.283
SER	A	47 HG1	35.344	28.389	22.814
LYS	A	210 CB	32.248	23.136	21.7
LYS	A	210 HB1	32.44	22.836	22.736
LYS	A	210 HB2	31.46	23.896	21.72
LYS	A	210 CG	33.52	23.732	21.078
LYS	A	210 HG1	33.4	23.878	19.998
LYS	A	210 HG2	34.351	23.027	21.202
LYS	A	210 CD	33.912	25.075	21.673
LYS	A	210 HD1	34.034	24.981	22.759
LYS	A	210 HD2	33.124	25.814	21.506
LYS	A	210 CE	35.247	25.562	21.118
LYS	A	210 HE1	35.994	24.769	21.174
LYS	A	210 HE2	35.637	26.403	21.685
LYS	A	210 NZ	35.227	26.014	19.715
LYS	A	210 HZ1	35.132	27.03	19.564
PHE	A	202 CA	31.509	32.626	15.652
PHE	A	202 HA	31.679	31.61	15.31
PHE	A	202 C	31.066	32.505	17.082
PHE	A	202 O	31.843	32.422	18.035
CYS	A	203 N	29.738	32.291	17.228
CYS	A	203 HN	29.099	32.666	16.538
HOH		402 O	35.297	29.007	19.553
HOH		402 H1	34.655	29.743	19.529
HOH		402 H2	35.765	29.105	20.421
RTAL		301 C1	41.013	29.34	10.326
RTAL		301 C2	41.593	30.413	9.367
RTAL		301 H21	41.876	31.293	9.956
RTAL		301 H22	40.798	30.755	8.69
RTAL		301 C3	42.752	29.901	8.522
RTAL		301 H31	43.559	29.515	9.158
RTAL		301 H32	43.182	30.707	7.919
RTAL		301 C4	42.232	28.783	7.63
RTAL		301 H41	43.051	28.282	7.101
RTAL		301 H42	41.609	29.205	6.826
RTAL		301 C5	41.418	27.751	8.376
RTAL		301 C6	40.871	27.97	9.613

RTAL	301 C7	40.162	26.866	10.261
RTAL	301 H71	40.012	25.985	9.646
RTAL	301 C8	39.687	26.785	11.534
RTAL	301 H81	39.82	27.621	12.206
RTAL	301 C9	38.957	25.685	12.123
RTAL	301 C10	38.455	25.913	13.382
RTAL	301 H101	38.671	26.889	13.812
RTAL	301 C11	37.625	25.092	14.2
RTAL	301 H111	37.396	24.071	13.904
RTAL	301 C12	37.11	25.618	15.358
RTAL	301 H121	37.359	26.653	15.577
RTAL	301 C13	36.321	24.963	16.353
RTAL	301 C14	35.941	25.734	17.44
RTAL	301 H141	36.093	26.804	17.366
RTAL	301 C15	35.553	25.244	18.7
RTAL	301 H15	35.623	24.183	18.924
RTAL	301 C16	41.961	29.212	11.546
RTAL	301 H161	42.022	30.174	12.068
RTAL	301 H162	42.967	28.917	11.236
RTAL	301 H163	41.622	28.473	12.272
RTAL	301 C17	39.642	29.893	10.784
RTAL	301 H171	38.928	29.904	9.956
RTAL	301 H172	39.771	30.924	11.123
RTAL	301 H173	39.191	29.346	11.611
RTAL	301 C18	41.306	26.466	7.592
RTAL	301 H181	42.24	25.899	7.673
RTAL	301 H182	41.185	26.701	6.53
RTAL	301 H183	40.485	25.807	7.875
RTAL	301 C19	38.729	24.409	11.358
RTAL	301 H191	38.228	24.596	10.403
RTAL	301 H192	38.113	23.708	11.921
RTAL	301 H193	39.684	23.917	11.135
RTAL	301 C20	35.918	23.524	16.19
RTAL	301 H201	36.748	22.875	15.905
RTAL	301 H202	35.183	23.45	15.381
RTAL	301 H203	35.45	23.125	17.09